TOWARD FIXTURELESS INSPECTION OF AUTOMOTIVE FENDERS

by

Corbin Michael Grohol

A thesis submitted to the faculty of
The University of North Carolina at Charlotte
in partial fulfillment of the requirements
for the degree of Master of Science in
Mechanical Engineering

Charlotte

2018

Approved by:

_____
Dr. Edward Morse

_____
Dr. Jimmie Miller

_____
Dr. Harish Cherukuri

ABSTRACT

CORBIN MICHAEL GROHOL. Toward fixtureless inspection of automotive fenders.
(Under the direction of DR. EDWARD MORSE)

With nonrigid parts, it is most convenient for designers to specify the desired

shape in the design condition; that is, the shape is specified with all loads present that the

part will experience in service (gravity, assembly constraints, etc.). The flexibility of the

part begins to pose challenges for the dimensional inspection of the part profile when the

deformations due to design loads exceed 10% of the dimensional tolerances. A common

approach to negotiate the inspection of nonrigid parts is to construct an inspection fixture

that mimics the design condition (identical mounting points and orientation to gravity).

Although effective, inspection fixtures have the limitation of cost, calibration

maintenance, procurement time, and the inspection is limited to a small subset of parts.

This thesis builds on the fixtureless inspection literature which has emerged in response

to these limitations.

The proposed fixtureless inspection method uses finite element simulations to

adjust the nominal design shape into the fixtureless measurement condition. Finite

element simulations are used to remove deformations from the nominal shape due to

design condition loads and add deformations due to measurement condition loads. In this

way, the part can be inspected under different constraints than the design condition and

without specialized fixtures. The details of the method are outlined including the finite

element simulations (using Abaqus), conditioning of the finite element mesh (using

MATLAB$^{®}$), optical point cloud acquisition (using a ROMER Absolute Arm with

integrated scanner), and the processing of the point cloud data (using MATLAB$^{®}$).

This method is first demonstrated on a cantilevered flat plate where the design condition is defined with a mass hanging on the end and the measurement condition is defined under the influence of gravity only. The proposed method is used to measure the profile deviation of the plate in the measurement condition (gravity only). For validation, the profile deviation is also measured in the design condition (mass hanging on the end). The profile deviation from the measurement condition is shown to match the directly measured profile deviation from the design condition to within 25 μm. This is two orders of magnitude lower than the 3 mm design condition deflections of the cantilevered plate.

The method is extended to an automotive fender where an original modal decomposition technique is used to deform the nominal model to the measurement data. The modal decomposition compensates for deformation of the part during assembly and provides a means to predict the required assembly forces. The profile deviation is measured using the proposed method with the fender in a fixtureless state resting on a flat table. For validation, the profile deviation of the fender is also measured in a specialized fixture to hold the fender in the design condition. The two profile deviations match within 0.6 mm, more than an order of magnitude lower than the 10 mm measurement condition deflections of the fender. This thesis provides one of the first automotive examples of fixtureless inspection and offers improved computational efficiency as finite element simulations for every measured part are not required.

ACKNOWLEDGEMENTS

TABLE OF CONTENTS

LIST OF TABLES

LIST OF FIGURES

CHAPTER 1: INTRODUCTION

1.1. Research area description

The assignment of geometric and dimensional tolerances to a part is a critical step in the design process and is intended to capture the precision with which the part must be manufactured. To assist in this endeavor, standards such as the ASME Y14.5 [1] have been developed. According to para. 4.20 of the ASME Y14.5 standard, unless otherwise specified, the manufactured part is dimensionally inspected in the free-state. ISO 10579:2010 defines the free-state as the part under the influence of gravity only. ASME Y14.5 provides exceptions to the free-state inspection rule for nonrigid parts in which the shape change is significant after the removal of manufacturing forces.

Abenhaim et al. [2] propose a compliance scale shown in Figure 1-1 to help contextualize the rigidity of a part. In zone A, parts are considered practically rigid. In this case, reasonable forces from handing and inspection (~40 N) cause deformations less than 5% of the part tolerances. In zone B, handling and inspection forces exceed 10% of the part tolerances and are classified as nonrigid. In Zone C, which includes parts such as gaskets and seals, parts are extremely nonrigid.
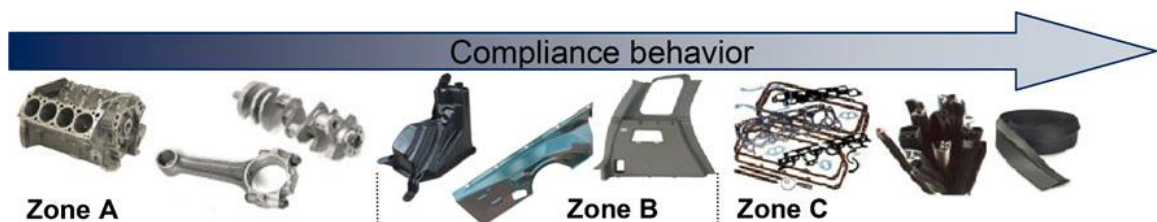
Figure 1-1: Compliance behavior scale (reproduced from Abenhaim et al. [2])

The research in this thesis investigates parts in the zone B category which pose unique challenges to dimensional specification and inspection. The challenge of the profile inspection of nonrigid parts in zone B is illustrated in Figure 1-2. Consider a

sheet-metal part of cylindrical-shell shape that is fastened to the bottom of an aircraft.

The designer defines the Computer Aided Design (CAD) model and the corresponding

profile tolerance when the part is on the aircraft. The design shape and profile tolerance

bounds appear as in Figure 1-2a where the arrows represent the fastening locations.

Dimensional inspection is completed off of the aircraft supported as shown in Figure

1-2b where the arrows represent the supports. The solid blue line represents the

manufactured part while the dotted line represents the ideal shape of the part with no

defects.
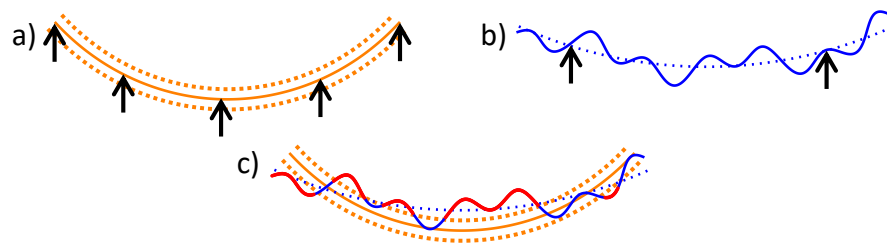
Figure 1-2: Cylindrical shell a) design condition CAD model, b) measurement data, and
c) evaluation of profile deviation

In Figure 1-2c, the CAD model and measured part are overlaid to evaluate the

profile deviation. Portions of the part that are outside of the tolerance zones are shown in

red. The part is out of tolerance partially due to gravitationally induced sag in the

measurement condition and partially due to actual manufacturing defects. In this

example, deviations due to manufacturing defects and gravitational sag are

indistinguishable.

1.2. Nonrigid specification

To deal with the challenge of the specification and inspection of nonrigid parts,

ASME Y14.5 provides exceptions to the free-state inspection requirement as defined in

para. 4.20 and 5.5. Abenhaim et al. [2] again provide a very useful classification structure

for navigating the nonrigid specification methods allowed by the ASME Y14.5 [1] standard which is reproduced in Figure 1-3.

The first specification method that departs from the free-state is the *restrained condition* which allows restraining features to impose deformations on the part during inspection. *Restrictive specification* is another method which allows the tolerance to be applied on a per unit basis to limit abrupt surface changes in a relatively short length. For example, the straightness of a 100 mm shaft may be controlled by applying a 0.1 mm straightness tolerance to any 25 mm zone along the length. The *restrictive specification* approach is described in ASME Y14.5 para. 5.4.1.3 for straightness and para. 5.4.2.2 for flatness. Lastly, *curved feature properties* allow the specification of curved properties such as arc lengths (see ASME Y14.5 para. 1.8.3).

The reader is referred to Abenhaim et al. [2] for a detailed explanation of each method. However, this brief explanation demonstrates that the *restrictive specification* and *curved feature properties* specification methods do not provide a means to evaluate the profile tolerance of a freeform part. As a result, the *restrained condition* is the only specification method well suited for the profile inspection of freeform nonrigid parts.

SPECIFICATION METHODS

UNLESS OTHERWISE SPECIFIED

FREE STATE | RESTRAINED CONDITION | RESTRICTIVE SPECIFICATION | CURVED FEATURE PROPERTIES

RESTRAINED ON A SHAPED FIXTURE | RESTRAINED BY MOVABLE DATUM TARGETS

RESTRAINED ON A HYPERSTATIC DATUM REFERENCE FRAME | RESTRAINED BY A FORCE

RESTRAINED ON A BASIC DIMENSION
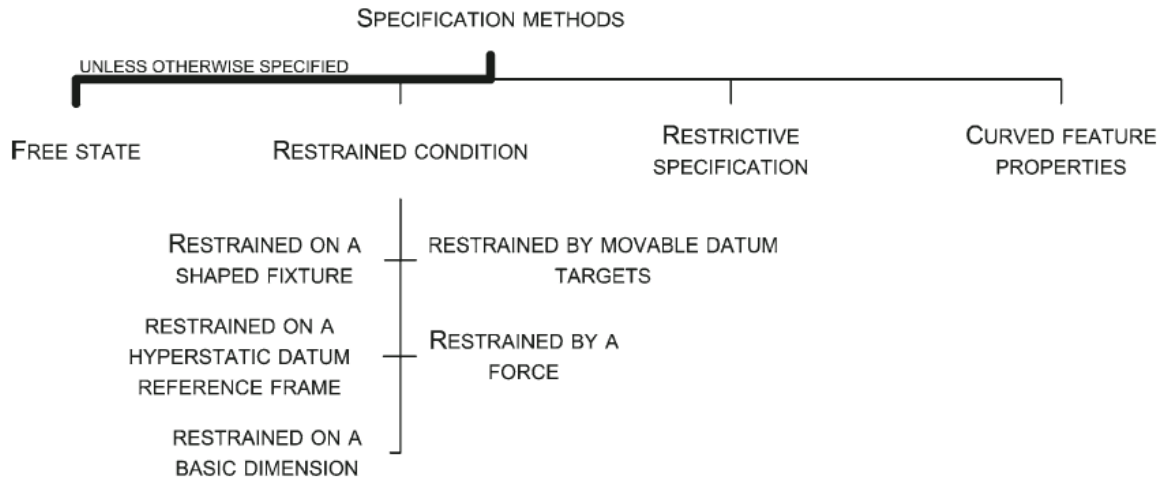
Figure 1-3: Categorization of inspection specification methods for nonrigid parts (reproduced from Abenhaim et al. [2])

1.3. Nonrigid inspection

All five of the *restrained condition* specification methods (shown in Figure 1-3) require the use of an inspection fixture. The most prevalent in the automotive and aerospace literature seems to be the *restrained on a shaped fixture* approach. In this method, a part of interest (hood, fender, aircraft skin, etc.) is mounted into a specialized fixture that holds the part in the *design condition* and measurements of the parts surface are captured using a 3D sensor. Reference points are used to rigidly transform the measurements and CAD model into the same coordinate system. The measured points on the part surface are then compared directly to the CAD model to determine if the part is in tolerance [3].

To illustrate the *restrained on a shaped fixture* approach, the cylindrical-shell part from Figure 1-2 is presented again in Figure 1-4. Instead of measuring in an arbitrary support condition (Figure 1-2b), a fixture is constructed to mimic the *design condition* (Figure 1-4b). The CAD model and measured part are overlaid to evaluate the profile

4

deviation in Figure 1-4c. Profile deviations due to gravitational sag are eliminated and the remaining deviations are therefore departures from the designer's intended shape.
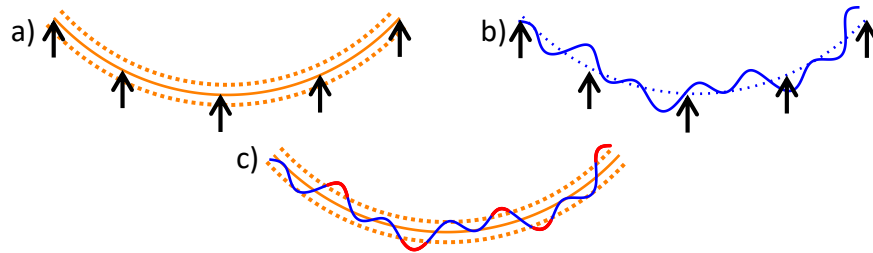
Figure 1-4: Cylindrical shell a) design condition CAD model, b) *restrained on a shaped fixture*, and c) evaluation of profile deviation

Ascione and Polini [4] provide an example in the literature of the *restrained on a shaped fixture* approach. They used the design drawings and datum structures from a helicopter winch fairing to design an inspection fixture shown in Figure 1-5 [4]. A high point-density inspection of the part was completed using a tactile-probe CMM. A total of 50,000 points were collected during the inspection and the measurement procedure was repeated five times. They demonstrated a repeatability (standard deviation) of 8.5 μm, much smaller than the profile tolerance of the part.
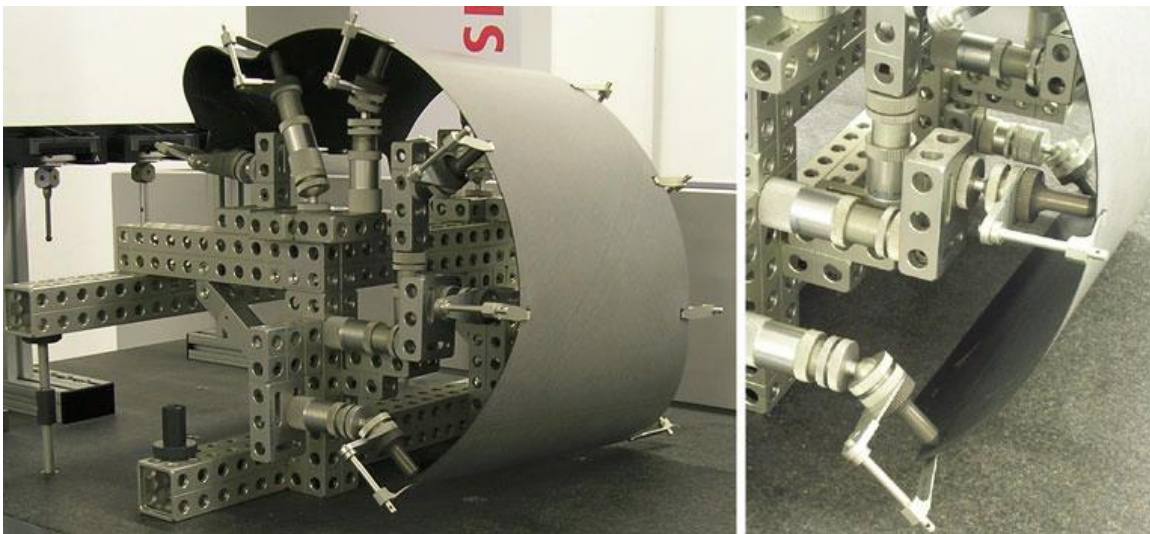
Figure 1-5: Measurement fixture for winch faring (reproduced from Ascione and Polini [4])

As shown by Ascione and Polini [4], the measurement repeatability and the limited number of uncertainty contributions no doubt make the *restrained on a shaped fixture* method a top choice for high quality inspection of nonrigid parts.

Although effective, as pointed out by many [2], [3], [5], the *restrained on a shaped fixture* method has several limitations including speed, cost, calibration maintenance, and procurement time. To help contextualize the cost and difficulty of maintaining a specialized fixture, consider an automotive fender with a 1 mm profile tolerance. The position of the fixture locations should be within 0.1 mm of the nominal design for the inspection equipment to be an order of magnitude more precise than the fender. Automotive fenders are of 1 m scale so the required fixture precision is 1 part in 10^4 (0.1 mm / 1 m). Additionally, automation is difficult and most inspection is performed manually on a small subset of parts.

In response to these limitations, a research area known as fixtureless inspection has emerged in an effort to eliminate these specialized inspection fixtures and enable 100% in-line profile inspection of nonrigid parts. This research area seeks to inspect parts in arbitrary support conditions. For example, a part may be inspecting lying on a table with no fixturing.

1.4. Fixtureless inspection literature review

Fixtureless inspection makes use of what Abenhaim et al. [2] termed *simulated displacement*. Simulations are either performed on the CAD model (defined in the *design condition*) or the scan data (measured in a fixtureless condition) to adjust the two data sets into the same condition. In either case, deformations due to gravity and the inspection fixture are virtually corrected for and the scan data is compared to the CAD

model to evaluate the dimensional conformance. The following paragraphs are intended to be a comprehensive review of the fixtureless inspection literature in roughly chronological order. The last paragraph of this section will summarize the current state of the literature and opportunities for improvement.

To the knowledge of the author, the earliest published research on fixtureless inspection was by Blaedel et al. [6] in 2002. They introduced the technical approach of inspecting the part in an arbitrary fixture and using simulation to remove the deformations due to the fixture, providing the shape of the part in its free state (i.e., floating in zero gravity). Another simulation is then completed to virtually deform the scan data from the free state into its functional equivalent that mimics the *design condition*. The distortion-compensated scan data is compared to the CAD model to evaluate the dimensional conformance. They created a useful diagram to represent their idea which is reproduced in Figure 1-6.
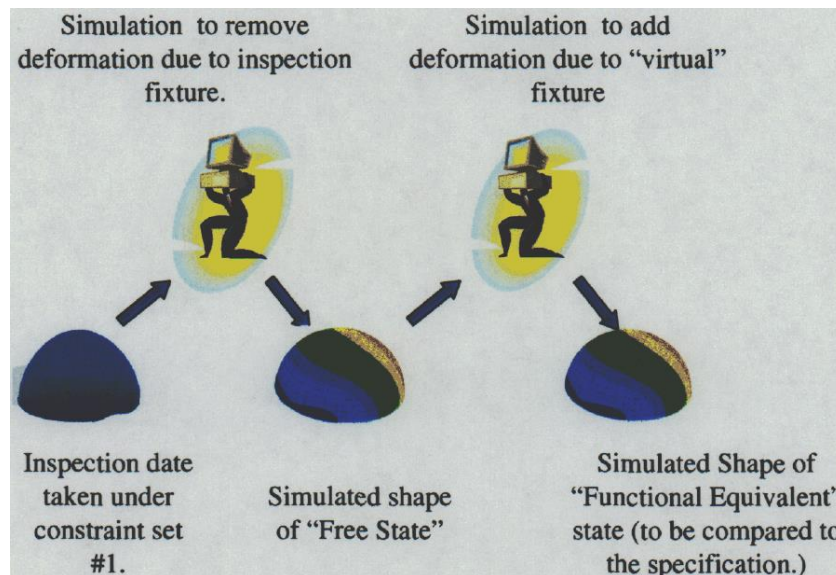
Figure 1-6: Technical approach by Blaedel et al. (reproduced from [6])

In 2005 and 2006, Weckenmann et al. [7], [8] published a method called *virtual distortion compensation*. They scanned the surface of a sheet metal part simply lying on a

7

table (fixtureless) using optical fringe projection measurement. A triangular mesh of the point cloud was created and feature extraction was used to locate the assembly features. Finite Element (FE) modeling was used to displace the assembly features to their nominal position. The distortion-compensated scan mesh was then compared to the CAD model. Their method corrected the profile of a sheet metal part from a profile deviation of about 6 mm in the fixtureless state to under 1 mm (in the interpretation of the author, this should be zero if the process worked perfect) in the distortion-compensated mesh.

In 2007, Weckenmann et al. [9] improved their previous method by performing the FE analysis on the CAD model rather than the scanned data in a *virtual reverse deformation* approach. The CAD model was meshed and FE boundary conditions were applied to move the fixation points of the CAD to the scanned data. This reduces the amount of processing that must be done on the scan data.

In 2009, Jaramillo et al. [10] sought to decrease the computational time of a method like the *virtual reverse deformation* approach to make the process more practical for in-line inspection (i.e., on an assembly line). Radial basis function interpolation was used to reduce the required mesh density in the FE calculations. They decrease the FE computation time by more than three orders of magnitude (from 282 seconds to 0.2 seconds). In 2011, they provide more details of the method along with additional case studies [3]. In 2013, they extended their method to only require partial scans of the inspected part [11], [12]. The partial view method was demonstrated on four plastic parts around 100 mm in size.

In 2010, Lemeš published a thesis [13] in which an uncertainty analysis and validation of the *virtual distortion compensation* approach was investigated. The method

was demonstrated on the diameter measurement of 25 deep-drawn-steel oil filter housings and 25 manually manufactured sheet-metal saddle brackets. Tensile tests were performed on 75 specimens to determine the statistical distribution of material properties. FE simulations were used to deform the fixtureless scanned part into the clamped configuration. A GOM ATOS II and NextEngine scanner were used for digitization of the parts. A GUM [14] based uncertainty analysis was completed on the 46 mm diameter oil filter housing and showed that a direct scanned measurement of the clamped part and the FE corrected fixtureless diameter measurement both yielded a measurement uncertainty of 93 μm (k = 2). This is an exciting result as it shows FE corrected measurements can be as precise as fixtured measurements.

In 2011, Gentilini and Shimada [15] used a method similar to *virtual distortion compensation* [7], [8] to predict the post assembly shape of a 500 mm scale plastic lid and a sheet-metal toaster housing. The pre-assembly shape of each part was attained using a 3D Laser Digitizer VIVID9i. The scanned shape was meshed and FE simulations were performed to deform the scan data into the assembly configuration to predict the post-assembly shape. A material calibration and boundary condition optimization process was also included. A comparison between the predicted post-assembly shape and actual scan data from the assembled parts showed average deviations around 0.3 mm with maximum deviations around ±4 mm.

Also in 2011, Abenhaim et al. [16] proposed a unique method which, unlike the previous studies, was not based on FEA. They named the method *iterative displacement inspection* algorithm. In this algorithm, the meshed CAD model is iteratively deformed until it matches the scanned manufactured part. The iterative deformation is done in such

a way to ensure the smoothness of the CAD surface so that neither the measurement noise nor surface defects of the manufactured part are concealed. Rather than scanning physical parts, they test their method on several simulated parts (300 mm to 1000 mm scale) with known defects. The simulated measurement data is created by adding a dent shape to the CAD model (about 3 mm profile deviation), performing FE analysis to deform the model from its nominal position (induced deformations around 30 mm), and adding measurement noise with a 0.1 mm standard deviation to the mesh. This is done 32 times on various 14 gauge (0.721 mm) aluminum parts. The detected profile deviations from their algorithm are within approximately 10% of the known simulated values. A drawback of this approach is it seems to be restricted to dent shaped profile deviations. In the same year, Aidibe et al. [17] added a maximum normed residual test to the algorithm to automatically set the identification threshold.

In 2012, Abenhaim et al. [2] published an excellent review on the specification and inspection of nonrigid parts. Their review of the subject was the source for much of the literature reviewed in this thesis.

Also in 2012, Radvar-Esfahlan et al. [18] introduce what they call the *generalized numerical inspection fixture* process to help generalize the procedure for fixtureless inspection. Their method is based on the distance-preserving property of nonrigid parts. They use the conservation of geodesic distance (shortest distance between two points along a surface) principle to identify corresponding points between the nominal CAD (fixtured) and scan data (fixtureless). FE analysis is then used to deform the CAD model to the scan data such that the identified corresponding points match. In a manner similar to Abenhaim et al. [16], they tested their method on simulated parts with known

displacements and bump shaped profile deviations. The reported errors in the results varied between less than 1% (detection of a 9.93 mm profile deviation for a known 10 mm bump) and over 25% (detection of a 1.44 mm profile deviation for a known 2 mm bump).

In 2014, the same authors (Radvar-Esfahlan et al.) increased the robustness of the *generalized numerical inspection fixture* process by filtering out incoherent geodesic distances from their similarity detection algorithm [19]. Incomplete scan data can be processed with the updated algorithm. Radvar-Esfahlan and Tahan [20] also completed a performance study of dimensionality reduction methods. Radvar-Esfahlan then organized these works into a doctoral thesis on *generalized numerical inspection fixtures* [21].

In 2013, Abenhaim et al. [22] performed a sort of best case analysis of the *virtual distortion compensation* approach [7], [8] where the properties of the material are known (no uncertainty), the thickness of the part is uniform and known (no uncertainty), and the position of the support points are known (no uncertainty). They perform the case studies on an aluminum aerospace panel of 2000 mm scale and 2.54 mm thickness. FEA is used to simulate a deformed fixtureless geometry before a variety of measurement noise distributions are imposed on the simulated fixtureless geometry. The appropriate FE boundary conditions are imposed on the simulated fixtureless geometry to force it into the nominal condition. The most interesting of the case studies is perhaps the *Predicted#2*. In this case, no measurement noise is added. The simulated fixtureless geometry is displaced to the nominal condition and compared to the nominal CAD model which results in a mean profile deviation of 0.027 mm and a maximum of 0.460 mm. Since this case consisted of no material property or measurement uncertainties, these

profile deviations represent the limit of the numerical accuracy of the FE analysis and the boundary condition definition.

In 2014, Aidibe and Tahan [23] introduced another non-FE based approach. They used Gaussian curvature properties, an intrinsic property of the part, in combination with a Thompson-Biweight statistical test to identify the profile deviations of nonrigid parts. The method is tested on three simulated parts and one experimental case with a variety of dent and waviness profile deviations. Their method properly identifies the deviations to within 2% to 17%, depending on the case. In 2015, the authors extend this method to include a *coherent point drift* algorithm [24]. In 2016, Babanezhad et al. [25] further improved this method with what they called a *bi-objective flexible registration* algorithm.

In 2015, Abenhaim et al. [26], [27] introduced a method that maps the scanned point cloud (from the fixtureless state) to the nominal model (fixtured state) using FEA results on the nominal model. In this way, all the FEA is performed on the nominal CAD avoiding the difficulties of generating a quality FE mesh from point cloud data. Abenhaim et al. [26] succinctly describe the process:

> This [point cloud mapping] is done by embedding a FE-based transformation model into a boundary displacement constrained optimization. The boundary displacement constrained optimization seeks to minimize a distance-based similarity criterion between points in unconstrained regions while maintaining a distance-based similarity criterion between points in constrained regions within a specified contact distance, and at the same time, limiting the restraining forces. [26]

Using simulated parts similar to ref: [22], the method results in shape errors 70% less than their previous work [22].

In 2016, Karganroudi et al. [28] improve on the *generalized numerical inspection fixture* [18] by filtering out inaccurate sample points. The *generalized numerical*

inspection fixture method generates a set of corresponding sample points between the scan data (fixtureless) and nominal CAD (fixtured) that are used to deform the CAD to the scan data by FE simulation. If some of the sample points are located close to the defects, the method can fail to detect those defects. In response to this issue, Karganroudi et al. use a curvature and von Mises stress filtering method to eliminate the sample points near the defects. They performed many case studies on simulated parts and, in general, the filtering method improves the estimation of defect size. In 2018, the authors asses the robustness of their method using a verification and validation approach [29]. In 2018, the authors also investigate the use of permissible restraining pressures for the fixtureless inspection of aerospace panels [30].

In 2017, Sabri published a thesis [31] documenting the works of Sabri et al. In 2016 and 2013, Sabri et al. [5], [32] presented a method very similar to the *generalized numerical inspection fixture* with the exception of the boundary condition definition for the FE analysis. When the corresponding points between the CAD model and scan data are found, only the points around fixating features (holes) are used. FE analysis is then used to displace the CAD model towards the scan data by applying translational displacement boundary conditions to the fixating features. They test their method on simulated parts with known defects. The performance ranges from a 0.3% to 25% error between the detected and known defect amplitude. In 2017, Sabri et al. [33] improved their previous method by increasing the accuracy of the displacement boundary conditions using an automatic FE node insertion technique. They retested on the simulated parts and reported minor improvements.

In 2017, Thiébaut et al. [34] presented a method based on a previous work [35] in which they dealt with the point cloud directly (i.e., no mesh of the scanned part was created). They used the mesh of the nominal CAD model to evaluate the point cloud. To evaluate the geometric deviation, they created a cylinder around the normal vector of each FE node. Cloud points within the cylinder were identified and the normal distance to the node for each identified cloud point was calculated. Then, the normal distances were averaged to attain a geometric deviation at that FE node. To attain the profile deviations, the geometric deviations were corrected for the FE calculated gravitational sag at each node. If the standard deviation or number of identified cloud points for a given node were too high, they ignored that node's data. Modal decomposition was used to develop a continuous function representation of the surface deviations to 1) interpolate the deviation where missing data existed and 2) enable assembly simulations. The method was tested on an aluminum sheet-metal section in multiple configurations and showed a repeatability of 0.02 mm over most of the part with differences reaching 0.06 mm in some areas.

As demonstrated, the literature on fixtureless inspection is fairly voluminous; however, it is certainly not closed. Below a few opportunities for remaining work in the fixtureless inspection of nonrigid parts are provided.

1) Recently, most of the proposed methods have only been tested on simulated data. While this is useful, when the methods are tested on real data, unforeseen obstacles will undoubtedly arise.

2) Other than the thesis of Lemeš [13], no rigorous uncertainty analysis has been completed. All the FE based methods are directly influenced by the part material properties and these influences should be quantified.

3) Large scale automotive parts such as hoods or fenders have yet to be studied.

4) Assembly forces have only been predicted in a few cases.

For these reasons, this thesis develops and original method for the fixtureless inspection of an automotive fender and predicts the assembly forces. Uncertainties in material properties and part thickness are considered for a simplified case study.

In the opinion of the author, the most intuitive method was that of Thiébaut et al. [34]. Interfacing directly with the scanned point cloud (no meshing of the point cloud necessary) and performing the FEA based off a known support configuration seemed achievable and was therefore chosen as the basis of the method for this thesis. This technique also implements FEA on the CAD geometry rather than the scan data and only requires FE simulations to be completed once for a given part design. In contrast, techniques that use FEA on the scan data require simulations for every measured part and would likely be infeasible in a production environment.

1.5. Thesis structure

Chapter 2 introduces the theory and nomenclature used in the proposed approach. Chapter 3 introduces the scanner used for point cloud acquisition. Chapter 4 applies the proposed approach to the profile deviation measurement of a flat plate. This case study provides an initial evaluation of the proposed approach on a simple geometry with boundary conditions that are simple to model. Chapter 5 estimates the uncertainty in the profile deviation measured in the Chapter 4 case study.

Chapter 6 conceptually investigates the proposed approach against a challenging measurement of a twisted plate. This investigation reveals limitations of the Chapter 2 formulation of the proposed approach. The proposed approach is modified with an original modal correction technique to account for over-constrained design conditions.

Chapter 7 implements the updated formulation of the proposed approach on the fixtureless inspection of an automotive fender. Finally, Chapter 8 will conclude the thesis, suggest opportunities for future work, and identify the research contributions of this thesis to the nonrigid inspection literature.

CHAPTER 2: PROPOSED APPROACH

For the remainder of the thesis, the *design condition* is defined as the condition in which the CAD model is specified. The *measurement condition* is defined as the fixtureless inspection configuration in which the part is measured. The *free condition* is defined as the shape of the part in zero gravity with all forces removed.

The goal of the proposed approach is to enable the measurement of the profile deviation (the measurand) of the manufactured part in an arbitrary "fixtureless" *measurement condition*. This avoids the cost and logistics of creating a dedicated fixture that holds the part in the *design condition* during inspection. Quotation marks are added to "fixtureless" to denote that some hardware may still be required to hold the part during measurement.

Continuing the cylindrical shell example from Figure 1-4, the proposed approach uses FEA to deform the CAD model (geometrically defined in the *design condition*) to the *measurement condition* as illustrated in Figure 2-1. Then, scan data from the *measurement condition* can be directly compared to the deformed CAD geometry to assess the profile deviation (measurand). The defect free part is represented by the orange solid line, the profile tolerance zone by the orange dashed line, the measured part by the blue line, and the out of tolerance regions in red. This approach only requires a simplified inspection stand (black arrows in Figure 2-1 *measurement condition*) as opposed to building a fixture to mimic the design condition as required in the *restrained on a shaped fixture* approach (recall Figure 1-4). Notice the proposed approach in Figure 2-1 reveals the same profile deviations (shown in red) as Figure 1-4 despite the differing support conditions.
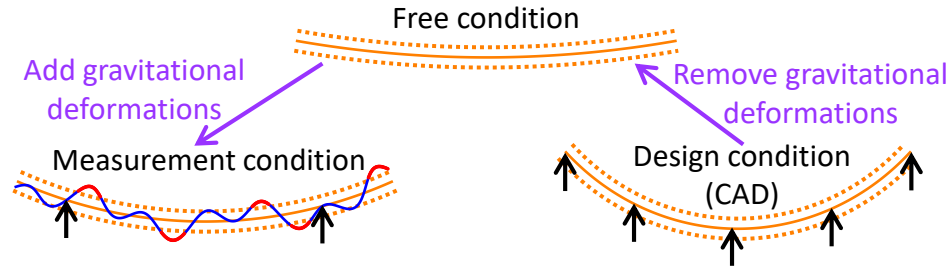
Figure 2-1: Principle of the proposed approach

The technique used in this thesis for the measurement of nonrigid parts was adapted from Thiébaut et al. [34]. It differs from Thiébaut et al. [34] through nomenclature changes and a modification to Equation (2.4) such that the profile deviation is evaluated by comparing the point cloud to the deformed *measurement condition* CAD model rather than the nominal *design condition* CAD model. Thiébaut et al. [34] also use the structural modes of the part to create an analytical representation of the profile deviation, which is not reproduced in this thesis.

2.1. Theory of proposed approach

In the following section, defect free surfaces are represented by S, deformations due to gravity as D, measured point clouds as M, and residual profile deviations (measurand) as R. Variables corresponding to the *design condition* carry the subscript *des* while *measurement condition* variables carry the subscript *meas*. S, D, and R correspond to the nodal coordinates of the discretized CAD model while M consists of the coordinates of the measured point cloud. The following paragraphs develop nomenclature and equations for the proposed approach which is illustrated in Figure 2-2.

18
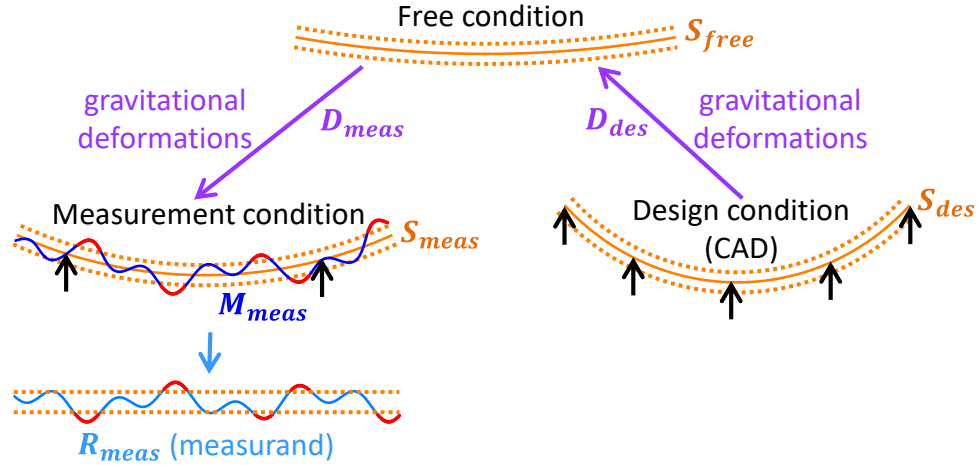
Figure 2-2: Nomenclature of proposed process

The shape of the design as captured by the CAD model in *design condition* is defined as S_{des}. It follows that the free shape of the component, when the forces of gravity and fixturing are removed, is defined as S_{free}. Defining the deformations due to gravity in the *design condition* as D_{des}, the relationship in Equation (2.1) is attained [34]. With the CAD model discretized into a mesh containing m nodes, S_{des} is an $mx3$ matrix containing the XYZ nodal coordinates of the *design condition* CAD model mesh. S_{free} is an $mx3$ matrix containing the XYZ nodal coordinates of the *free condition* (gravity and fixturing forces removed) mesh. D_{des} is an $mx3$ matrix obtained from FE simulations containing the dXdYdZ nodal displacements due to *design condition* gravity. D_{des} thus represents the displacements necessary to deform S_{free} to S_{nom} as captured in Equation (2.1) [34].

$$S_{des} = S_{free} + D_{des} \qquad (2.1)$$

The defect-free surface in the *measurement condition* is defined as S_{meas} as captured by Equation (2.2). S_{meas} is an $mx3$ matrix containing the XYZ nodal coordinates of the *measurement condition* CAD model mesh. D_{meas} is an $mx3$ matrix

19

obtained from FE simulations containing the dXdYdZ nodal displacements due to *measurement condition* gravitational load and represents the displacements necessary to deform S_{free} to S_{meas}. Combining Equation (2.1) and (2.2) to produce Equation (2.3), S_{meas} is attained by taking the *design condition* CAD model (S_{des}), subtracting *design condition* (D_{des}) displacements, and adding *measurement condition* (D_{meas}) displacements. This is illustrated in Figure 2-2.

$$S_{meas} = S_{free} + D_{meas} \tag{2.2}$$

$$S_{meas} = S_{des} - D_{des} + D_{meas} \tag{2.3}$$

Now, the manufacturing induced deviations from the ideal geometry can be discussed. In this proposed approach, the profile deviations (the measurand) are attained by measuring the part shape in an arbitrary "fixtureless" configuration using non-contact optical scanning. The scanning generates a point cloud with p points defined as M_{meas} which is a $px3$ matrix containing the XYZ coordinates of the point cloud and contains deformations due to the *measurement condition* gravity and profile deviations.

The residual profile deviations (the measurand) due to the manufacturing process are defined as R_{meas} which is an $mx1$ matrix containing the surface normal distance between the *measurement condition* CAD model (S_{meas}, Equation (2.3)) and the scanned part surface (M_{meas}). This is illustrated in Figure 2-2.

R_{meas} can be *conceptually* represented in Equation (2.4). However, the matrices are different sizes and the surface normal distance needs to be computed so the equation is not strictly executable. A method for evaluating Equation (2.4) will be discussed in the next section.

$$R_{meas} = M_{meas} - S_{meas} \tag{2.4}$$

2.2. Profile deviation calculation

The following section provides a means for evaluating the profile deviation (R_{meas}) given the conceptual basis of Equation (2.4). This method is directly from Thiébaut et al. [34] except for 1) different nomenclature and 2) Thiébaut et al. evaluate R_{meas} by comparing M_{meas} to S_{des} (and then correct for FE predicted deformations later) whereas here M_{meas} is compared to S_{meas} (already takes FE predicted deformations into account). The two approaches should lead to the same result; however, the author believes the approach in this thesis is more intuitive and slightly more computationally efficient.

Figure 2-3 (adapted from Thiébaut et al. [34]) depicts the stages of the calculation of R_{meas}. The step by step procedure is described as follows (adapted from Thiébaut et al. [34]):

1) The measured point cloud (M_{meas}) is registered to the *measurement condition* CAD surface (S_{meas}). The rough registration is completed through aligning the two coordinate systems while the fine registration is accomplished through a rigid-body best-fit transformation. An example result is shown in Figure 2-3a.

2) The normal vector ($\vec{n}_i$) of each node (S_{meas_i}) is calculated (see Figure 2-3b). Here, i is the index into the m nodes. The details of the nodal normal vector calculation can be found in Appendix A.1.

3) For the ith node, a cylindrical zone of radius R is defined around $\vec{n}_i$. Nearest neighbors from the M_{meas} point cloud within the cylindrical zone are identified as N (see red points in Figure 2-3b). N is a $q x 3$ matrix containing the XYZ coordinates of each of the nearest neighbors. q is the number of nearest neighbors

for the ith node. The details of the nearest neighbor search can be found in Appendix A.2.

4) The surface normal distance $e_{ik} = \overrightarrow{S_{meas_i} N_k} \cdot \vec{n}_i$ is calculated for each nearest neighbor cloud point N_k (see Figure 2-3c). Here, k is the index into the q nearest neighbors of the ith node.

5) The residual profile deviation $R_{meas_i} = mean(e_i)$ (measurand) is calculated for each node resulting in an $mx1$ matrix of profile deviations. As a result, every node of the S_{meas} mesh has a corresponding profile deviation.

6) As a measure of scan noise, the standard deviation of the nearest neighbor surface normal distances is calculated $\sigma_i = \sqrt{\frac{1}{q-1}\sum_{k=1}^{q}(e_{ik} - R_{meas_i})^2}$.

7) As a measure of scan density, the number of nearest neighbors per node is stored $Q_i = q$.

8) If σ_i is above a threshold (0.05 mm in this thesis) or Q_i is below a threshold (10 in this thesis), the point cloud (M_{meas}) at that node (S_{meas_i}) is deemed too noisy or insufficiently dense to trust its representation of the part surface. Thus, the profile deviation R_{meas_i} is ignored for that node. This step will create some missing data in the residual profile deviation field (R_{meas}). This is where Thiébaut et al. [34]) used modal decomposition to interpolate the missing data, which is not reproduced in this thesis.
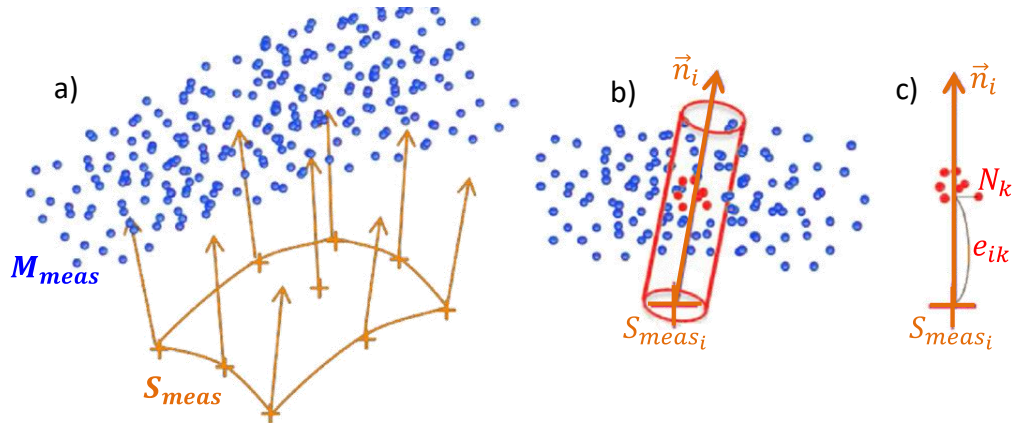
Figure 2-3: Evaluation of $\boldsymbol{R_{meas}}$ by a) registration of scan data to CAD, b) identification of nearest neighbors, and c) calculation of the profile deviation (adapted from Thiébaut et al. [34])

The resulting measurand (the residual profile deviation $\boldsymbol{R_{meas}}$) reveals the manufacturing defects that cause the real part to differ from the ideal defect-free geometry ($\boldsymbol{S_{meas}}$). These defects have to be evaluated against the profile tolerance to determine if the part is acceptable. Since $\boldsymbol{S_{meas}}$ is corrected for gravitational sag in the *design* and *measurement conditions* (recall Equation (2.3)), $\boldsymbol{R_{meas}}$ allows direct access to the manufacturing defects. That is, the challenges of separating gravitational effects from manufacturing defects previously shown in Figure 1-2 are overcome using the proposed approach.

The MATLAB code for accomplishing the profile deviation calculation is provided in Appendix A.3.

2.3. Performance check

If the proposed approach were implemented in an industrial setting, $\boldsymbol{R_{meas}}$ would serve as the final measurand and no additional work would be required. In this thesis however, additional measurements will be performed to evaluate the proposed approach against the common *restrained on a shaped fixture* approach (recall Figure 1-4).

The proposed approach and the *restrained on a shaped fixture* approach will be executed in parallel as shown in Figure 2-4. The part will be mounted in an inspection fixture that holds it in the *design condition*. The part will then be scanned to attain a point cloud $\boldsymbol{M_{des}}$. The profile deviation $\boldsymbol{R_{des}}$ will be calculated just as in section 2.2 by comparing $\boldsymbol{M_{des}}$ to $\boldsymbol{S_{des}}$ (*conceptually* represented in Equation (2.5)). In an ideal case, $\boldsymbol{R_{meas}}$ and $\boldsymbol{R_{des}}$ would match perfectly. The performance of the proposed approach will be judged on how closely they match.

$$R_{des} = M_{des} - S_{des} \tag{2.5}$$
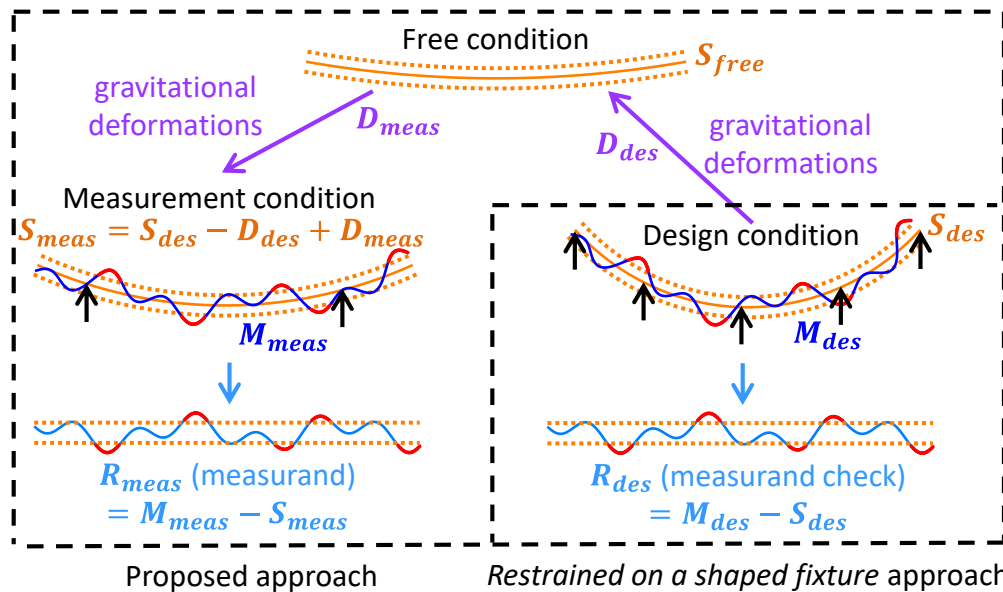
Figure 2-4: Parallel execution of the proposed approach and the *restrained on a shaped fixture* approach

CHAPTER 3: DATA ACQUISITION

The proposed approach requires an input point cloud ($\boldsymbol{M_{meas}}$). There are many methods for non-contact point cloud acquisition as detailed in Savio et al. [36] and Li and Gu [37]. In this thesis, a ROMER Absolute Arm with integrated laser-line scanner is used. The UNC Charlotte Center for Precision Metrology owns one and the versatility of the contact stylus and scanner in one measurement system is convenient for this laboratory scale experiment. The metrology software Spatial Analyzer was used to operate the ROMER Arm during data acquisition. For full production automation, an automated fringe projection scanner is more appropriate.

The ROMER Arm is shown in Figure 3-1. The specifications directly from the product brochure for the ROMER Absolute Arm are provided in Table 3-1. The single point repeatability and volumetric accuracy are evaluated according to the ASME B89.4.22 standard for performance evaluation of articulated arm coordinate measuring machines. Currently, there is no standardized test for scanner performance.

The single point repeatability test involves measuring a point from multiple approach directions. The value reported is the maximum deviation from the average of the recorded points. The volumetric accuracy test involves measuring a calibrated length standard in several locations and orientations. The value reported is the maximum deviation between the measured lengths and the certified length. The scanning system accuracy test involves measuring a matte sphere from five different articulated positions. The value reported is the maximum center-to-center distance of the five sphere scans. (source: HexagonMI.com)

Figure 3-1: ROMER Absolute Arm with integrated RS4 scanner (source:
HexagonMI.com)

Table 3-1: ROMER Absolute Arm with integrated RS4 scanner specifications (source:
HexagonMI.com)

Model #	RA-7525SEI-4
Date of manufacture	May 2016
Single point repeatability	0.027 mm
Volumetric accuracy	±0.038 mm
RS4 scanning system accuracy	0.063 mm
RS4 scanning sensor accuracy	0.028 mm (2σ)

CHAPTER 4: CASE STUDY - CANTILEVERED FLAT PLATE

The first case study of the proposed approach was completed on a cantilevered aluminum flat plate 313.68 mm x 101.63 mm x 2.479 mm in size (22 μm uncertainty in length and width, 11 μm uncertainty in thickness). The goal of this case study was to assess the performance of the proposed process as discussed in section 2.3. Ideally, the profile deviation measured using the proposed process in the *measurement condition* (R_{meas}) would match that measured in the *design condition* (R_{des}). This case study provides a simple geometry with simple boundary conditions for the first test of the proposed approach.

4.1. Setup and point cloud acquisition

The nominal plate geometry was defined as perfectly flat in the *free condition* (S_{free}). The plate was mounted in a cantilevered support such that the overhanging dimensions were 221.68 mm x 101.63 mm x 2.479 mm. Using the touch probe of the ROMER Arm, a coordinate system was created (see Figure 4-1a).

Two arbitrary loading conditions that would produce significantly different plate shapes were chosen as the *design* and *measurement conditions*. The *design condition* defect-free surface (S_{des}) was defined as the plate in a cantilevered support with a 739.8 g mass hanging at the top right corner of the plate (see Figure 4-1b). The *measurement condition* defect free surface (S_{meas}) was defined as the plate under the influence of gravity only (see Figure 4-1a).

Figure 4-1: Flat plate in a) *measurement condition* and b) *design condition*

The point clouds in Figure 4-2 were acquired with the plate loaded as shown in Figure 4-1. A point cloud (M_{meas}, Figure 4-2a) of 500,514 points was acquired in the *measurement condition* using the ROMER Arm RS4 scanner. The vertical structures at x = 220 mm in Figure 4-2a are simply the cloud points measured in the tapered holes. The mass was applied to the top right corner and another point cloud (M_{des}, Figure 4-2b) of 634,525 points was acquired in the *design condition*.
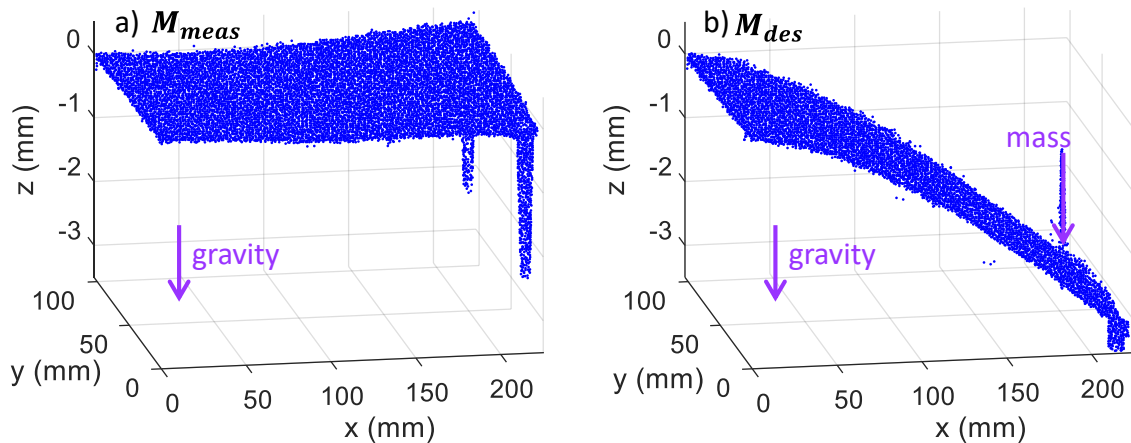
Figure 4-2: Unprocessed point clouds in a) *measurement condition* and b) *design condition*

4.2. FE analysis

To create the *design condition* CAD mesh (S_{des}), an FE simulation was carried out in Abaqus. A shell part of size 221.682 mm x 101.630 mm was created. The part was assigned aluminum material properties of Young's modulus 69×10^9 Pa, Poisson's ratio

0.35, and density 2700 kg/m³. The shell was assigned a thickness of 2.479 mm and the default Simpson integration rule with 5 integration points was used. A fixed boundary condition was applied along the x = 0 edge restricting displacement and rotation about all three axes. A gravitational load of -9.7976 m/s² was applied in the z direction. To represent the mass, a concentrated force of 0.7398 kg x -9.7976 m/s² = -7.2483 N was applied at the x = 221.682 mm, y = 101.630 mm corner node in the z direction.

Quadrilateral shell elements were creating by seeding the edges with 4 elements along each edge creating a 16 element mesh. The simulation was executed and the displacement of the x = 221.682 mm, y = 101.630 mm corner node with the mass was recorded. To evaluate the sufficiency of the mesh density, the number of elements was doubled along each edge and the simulation was re-executed reporting the displacement each time. This was repeated until the displacement sufficiently converged. The results of the mesh convergence can be found in Table 4-1 and graphically represented in Figure 4-3. The transition from 1024 to 4096 elements only resulted in a 2 μm change in displacement. This is much less than the volumetric accuracy of the scanner and was deemed sufficiently converged. The final mesh used for the FE simulations is shown in Figure 4-4 and resulted in 4255 nodes.

Table 4-1: Total elements versus nodal displacement of the weighted node

Elements per edge	Total elements	Weighted node displacement (mm)
4	16	-3.075
8	64	-3.108
16	256	-3.118
32	1024	-3.123
64	4096	-3.125
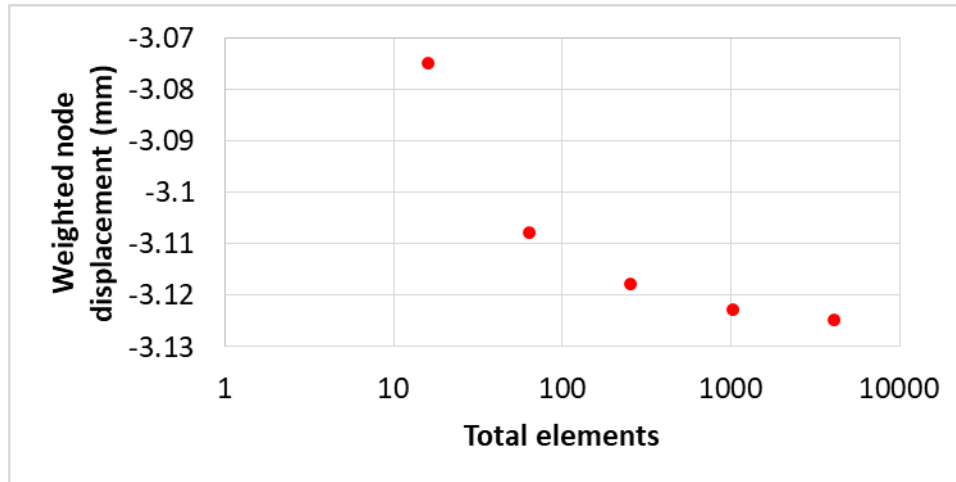
Figure 4-3: Total elements versus nodal displacement of the weighted node
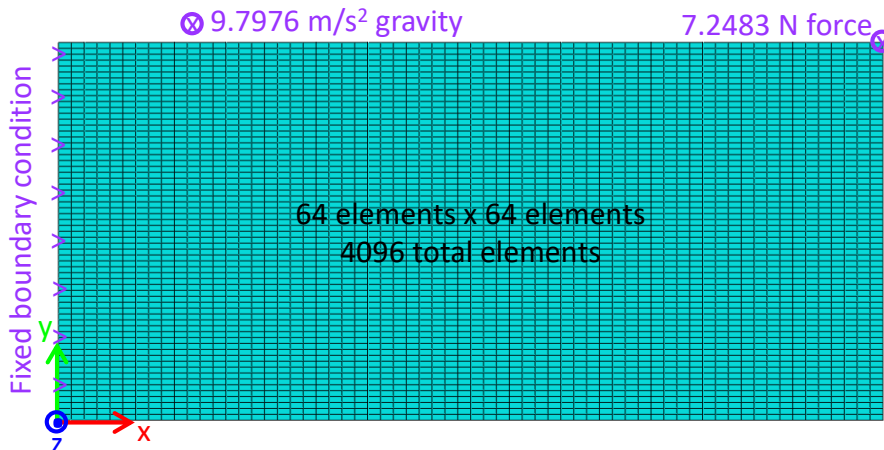
Figure 4-4: Mesh used for FE simulations (*design condition* loads shown)

The FE simulation was executed using the 4255 node mesh. The *free condition* nodal coordinates (S_{free}) were attained from the Abaqus *.inp* file. The nodal displacements representing deformations due to the *design condition* loads (D_{des}) were exported from Abaqus. According to Equation (2.1), D_{des} was added to S_{free} to attain S_{des}.

An FE simulation was completed for the *measurement condition* using all the same settings except the concentrated force representing the mass was removed. The nodal displacements representing deformations due to the *measurement condition* loads

($\boldsymbol{D}_{meas}$) were exported from Abaqus. The *measurement condition* CAD mesh ($\boldsymbol{S}_{meas}$) was calculated according to Equation (2.2).

The deformed meshes are shown in Figure 4-5 and Figure 4-6. The maximum displacement in the *measurement condition* was -0.21 mm. The maximum displacement in the *design condition* was -3.30 mm.
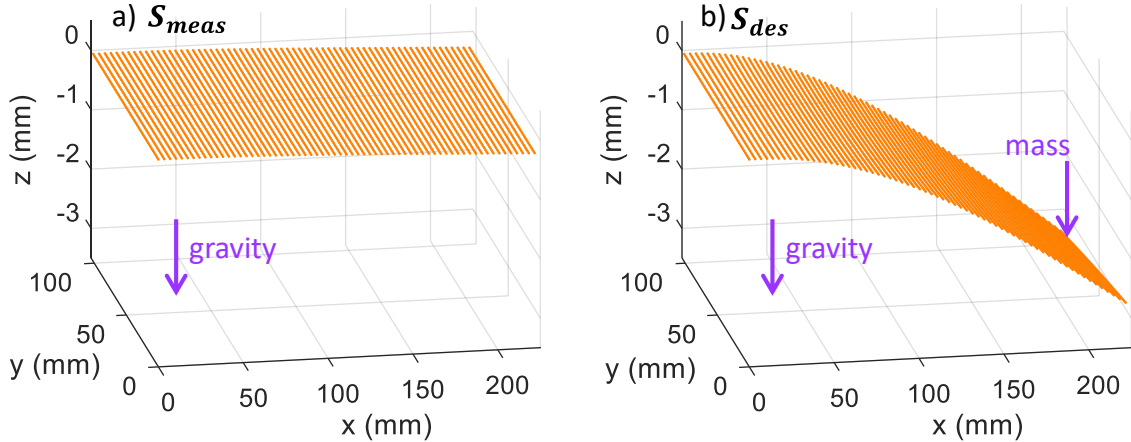
Figure 4-5: Deformed FE meshes in a) *measurement condition* and b) *design condition*
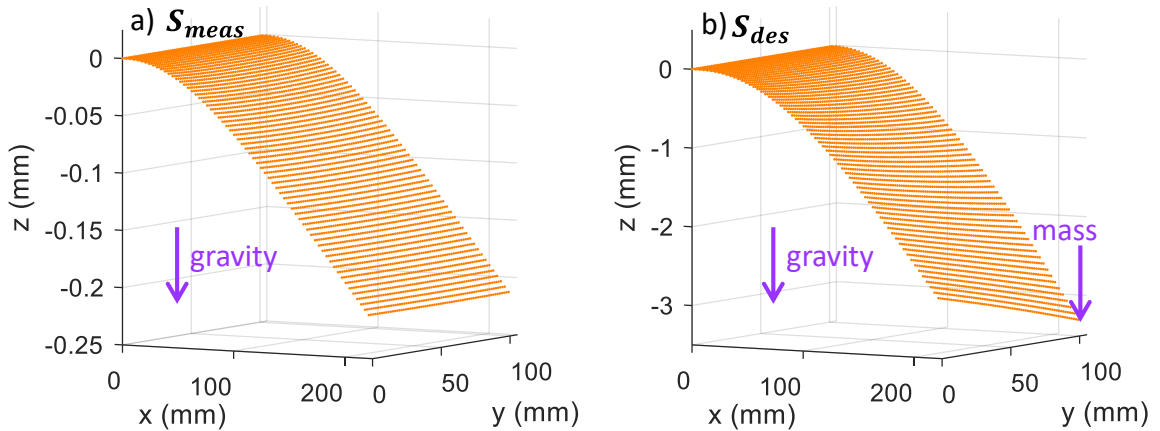
Figure 4-6: Deformed FE meshes reproduced from Figure 4-5 with different orientations and scaling

4.3. Point cloud registration

According to step 1) of the profile deviation calculation (recall section 2.2), the measured point cloud must be registered to the CAD mesh. To accomplish this task, it is first necessary to simplify the point cloud such that there exists a one-to-one CAD node

31

to point cloud correspondence. This was accomplished by creating a 1 mm cylinder that extended along the z direction at each node. Cloud points within the cylinder were averaged to create a single cloud point for each node. The MATLAB code is provided in Appendix B.1.

The X-Y-yaw alignment was deemed satisfactory due to the coordinate system setup with the ROMER Arm touch probe during data acquisition. However, the clamping system (Figure 4-1), is believed to provide insufficient restraint to pitch-roll movements. As such, the simplified point clouds were transformed to their corresponding CAD mesh (simplified M_{meas} to S_{meas}, simplified M_{des} to S_{des}) by minimizing the sum of the squared z distances through z-roll-pitch movements. The MATLAB code is provided in Appendix B.2. The resulting simplified point clouds transformed to their corresponding CAD meshes are shown in Figure 4-7 and begin to reveal the profile deviation. Note, the transformations were applied to the entire point clouds (Figure 4-2), even though the simplified point clouds are shown in Figure 4-7 just for neatness.
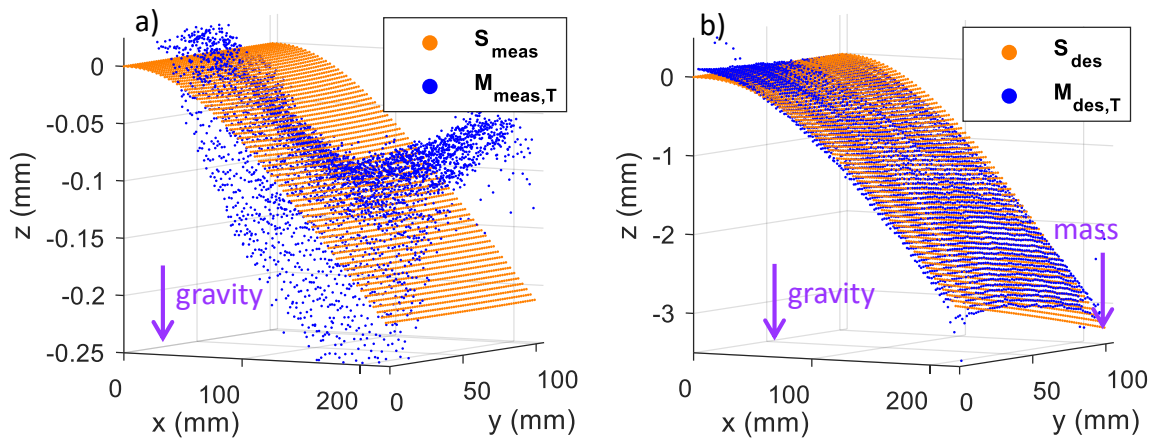
Figure 4-7: Transformed point clouds from a) *measurement condition* and b) *design condition*

4.4. Profile deviation calculation

Next, according to steps 2) through 8) the profile deviation was calculated using the MATLAB code in Appendix A.3. The cylindrical search radius (R) was set to 1 mm, the standard deviation (σ_i) threshold to 0.05 mm, and the nearest neighbor (Q_i) threshold to 10. $\boldsymbol{R_{meas}}$ (500,514 points and 4,225 nodes) took 344 seconds of CPU time and $\boldsymbol{R_{des}}$ (634,525 points and 4,225 nodes) took 429 seconds. The calculations were performed on a ThinkPad T530 laptop with an Intel® Core i7-3720QM CPU @ 2.60 GHz.

The resulting profile deviation is presented in Figure 4-8. The profile deviation reveals a 0.2 mm deviation around (200 mm,100 mm) as well as an overall saddle shaped deviation with the saddle point near (100 mm, 50 mm). If the proposed process worked perfectly, the measurand ($\boldsymbol{R_{meas}}$) and the measurand check ($\boldsymbol{R_{des}}$) would be identical. Qualitatively, they do look similar.
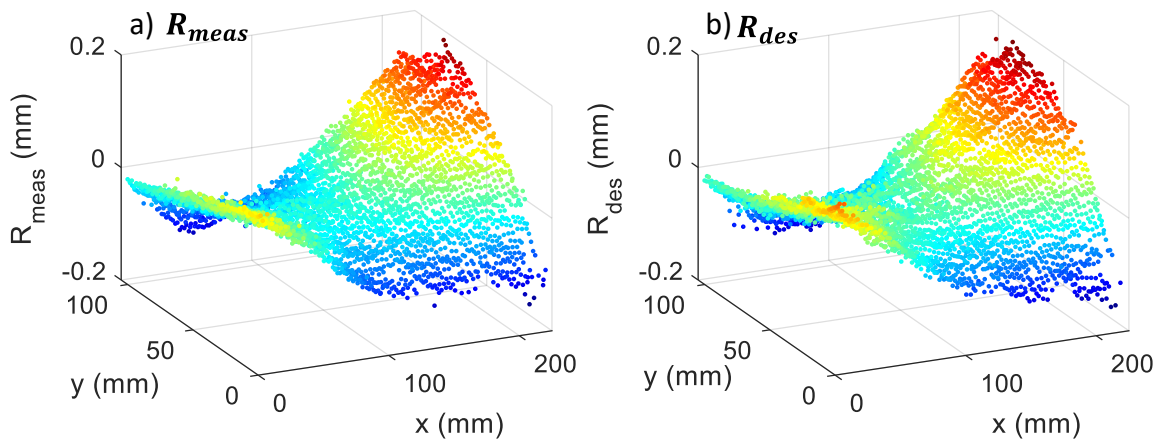
Figure 4-8: Profile deviation from a) *measurement condition* (measurand) and b) *design condition* (check of measurand)

The difference between $\boldsymbol{R_{meas}}$ and $\boldsymbol{R_{des}}$ is presented in Figure 4-9. The statistics relating to the difference are listed in Table 4-2. 95% of the deltas lie within ±25 μm. These deltas will be investigated through an uncertainty analysis in Chapter 5.
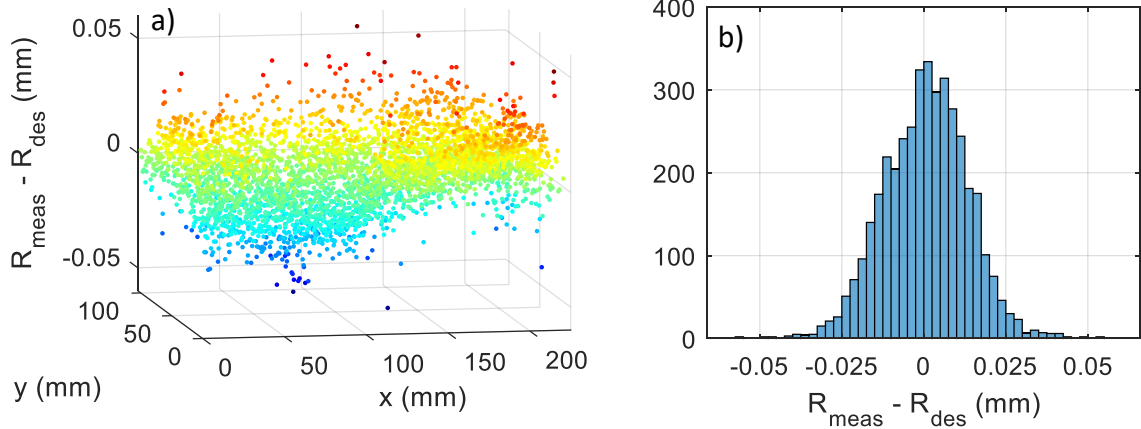
Figure 4-9: Deltas between R_{meas} (measurand) and R_{des} (check of measurand) represented a) graphically and b) in a histogram

To help contextualize the magnitude of the deltas, the simplified M_{des} point cloud was transformed to the simplified M_{meas} point cloud as shown in Figure 4-10. This comparison shows that the deformations due to gravity and the applied weight caused shape differences in the flat plate that ranged from -0.4 mm to 0.2 mm. The proposed approach was able to realize the profile deviations from two different loading conditions within ±25 µm (recall discussion on Figure 4-9) in the background of these 0.4 mm shape differences (Figure 4-10). The proposed method is therefore able to identify profile deviations an order of magnitude better than the background shape differences. This result is considered a success for the first case study.
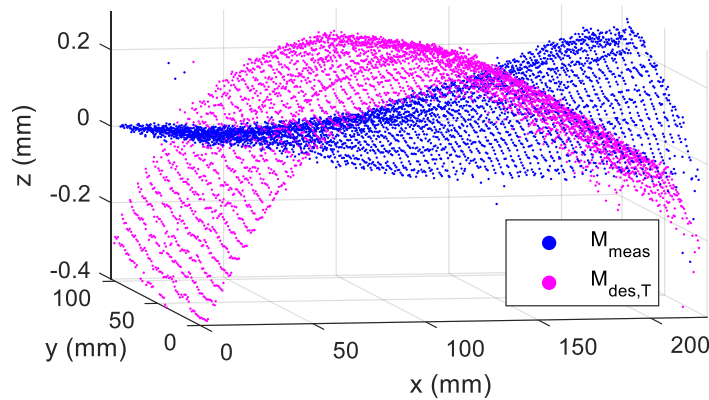
Figure 4-10: M_{des} (*design condition*, gravity and weight) simplified point cloud transformed to M_{meas} (*measurement condition*, gravity only) simplified point cloud

Table 4-2: Statistics relating to profile deviation calculation results

Variable		Mean	Std. dev.	Min	Percentiles				Max
					2.5%	16%	84%	97.5%	
R_{meas} - R_{des} (mm)		0.001	0.013	-0.057	-0.024	-0.012	0.013	0.025	0.054
Measurement condition	σ_i (mm)	0.034	0.160	0.000	0.013	0.016	0.027	0.043	2.882
	Q_i	53.6	28.7	0	9	25	80	119	226
Design condition	σ_i (mm)	0.033	0.134	0.000	0.013	0.016	0.028	0.048	2.899
	Q_i	77.3	38.4	0	19	40	111	157	453

The standard deviation per node, as calculated in step 6), is shown for the

measurement condition in Figure 4-11. From Table 4-2 the mean is 0.034 mm. As

mentioned at the beginning of this section, the standard deviation threshold was set to

0.05 mm. As a result, any node with a standard deviation greater than 0.05 mm was

ignored and a profile deviation value was not calculated. Figure 4-11a reveals that most

of the large standard deviations occur near the edges or holes of the plate where the point

cloud becomes distorted. From Table 4-2 and Figure 4-11b, 95% of the standard

deviations were between 0.013 mm and 0.043 mm. These standard deviations are

reasonable given the specified accuracy of the scanner (Chapter 3).
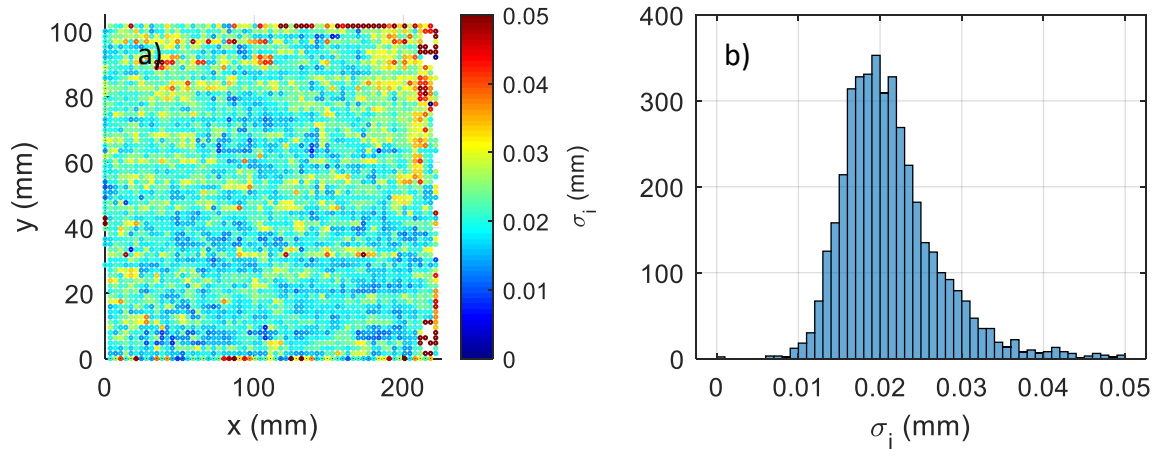
Figure 4-11: The standard deviation per node for the *measurement condition* (gravity only) represented a) graphically and b) in a histogram

The number of nearest cloud point neighbors within the cylindrical search volume, as calculated in step 7), is shown for the *measurement condition* in Figure 4-12. From Table 4-2 the mean is 53.6. The number of nearest neighbors threshold was set to 10 resulting in any node with fewer than 10 neighboring cloud points being ignored. Given that point cloud acquisition with the ROMER Arm is a manual process, the distribution of nearest neighbors shown in Figure 4-12a is inhomogeneous. From Table 4-2 and Figure 4-12b, 95% of the nearest neighbor counts were between 9 and 119.
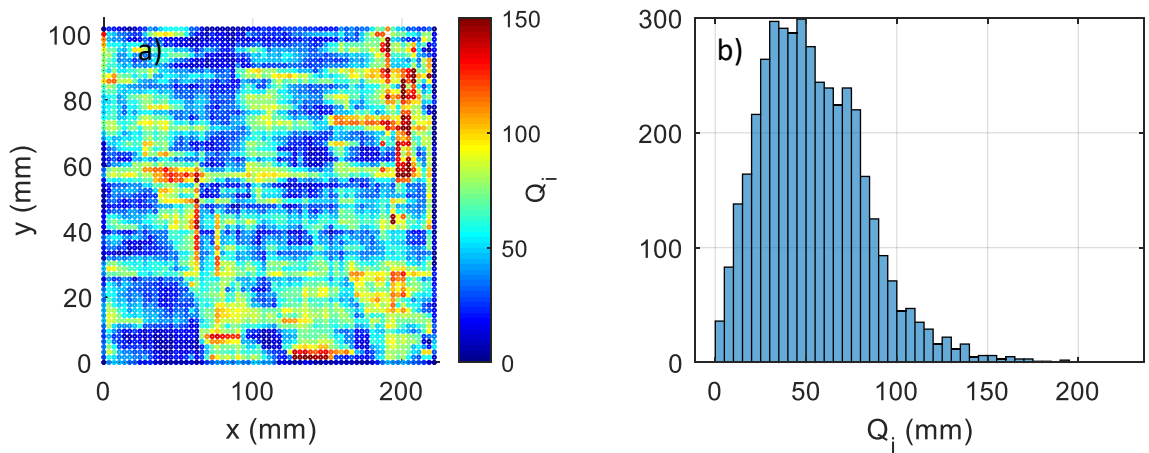
Figure 4-12: The number of nearest cloud point neighbors per node for the *measurement condition* (gravity only) represented a) graphically and b) in a histogram

The standard deviation and nearest neighbor threshold checks from step 8) of the profile deviation calculation produce gaps in the profile deviation field. The previously shown R_{meas} in Figure 4-8a is reproduced in Figure 4-13 from a vertical view to show the gaps. In Thiébaut et al. [34] modal decomposition is used to produce a continuous function representing the profile deviation. The function is then used to interpolate the profile deviation in the presence of the gaps.
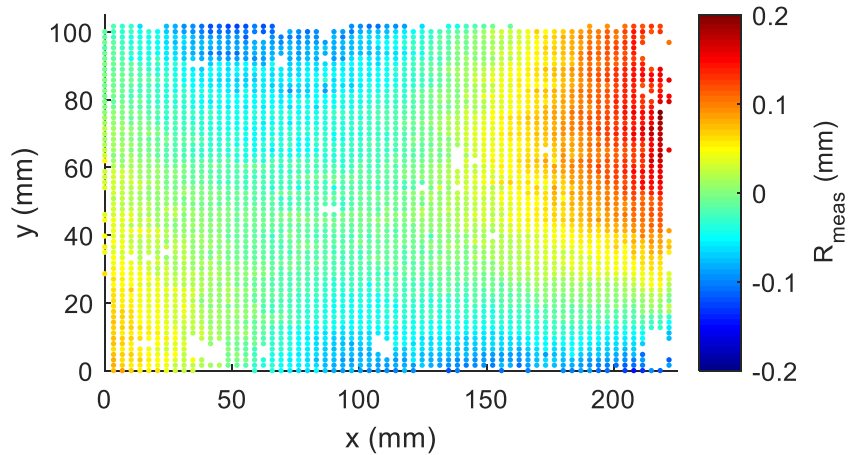
Figure 4-13: Profile deviation from *measurement condition* (measurand) showing gaps in the profile deviation field

4.5. Cantilevered flat plate conclusion

As a reminder, the goal of the proposed process is to measure the profile deviation (R_{meas}) in a simplified *measurement condition* and predict the prolife deviation (R_{des}) in the more complicated *design condition*. This way, the part only needs to be measured in the *measurement condition* and no specialized fixture is needed to replicate the *design condition*. The proposed approach is judged by how closely R_{meas} and R_{des} match.

Figure 4-14 reviews the steps in the cantilevered flat plate case study. This figure matches the generic performance check process from Figure 2-4. S_{free} was defined as perfectly flat. S_{des} and S_{meas} were calculated by adding their corresponding deformations D_{des} and D_{meas}. The point clouds M_{meas} and M_{des} were registered to the defect free surfaces S_{des} and S_{meas}. The profile deviation calculation (section 2.2) was performed to produce the profile deviation fields R_{meas} and R_{des}. Finally, R_{meas} and R_{des} were compared.

Figure 4-9 and Table 4-2 demonstrated that for the flat plate case study 95% of the deltas between R_{meas} and R_{des} were within ±25 μm. This is an order of magnitude

37

smaller than the background shape differences (Figure 4-10) and two orders of magnitude

smaller than the background *design condition* deflections (Figure 4-7b). Uncertainties in

each step of the proposed approach are the reason $\boldsymbol{R_{meas}}$ and $\boldsymbol{R_{des}}$ do not match

perfectly.
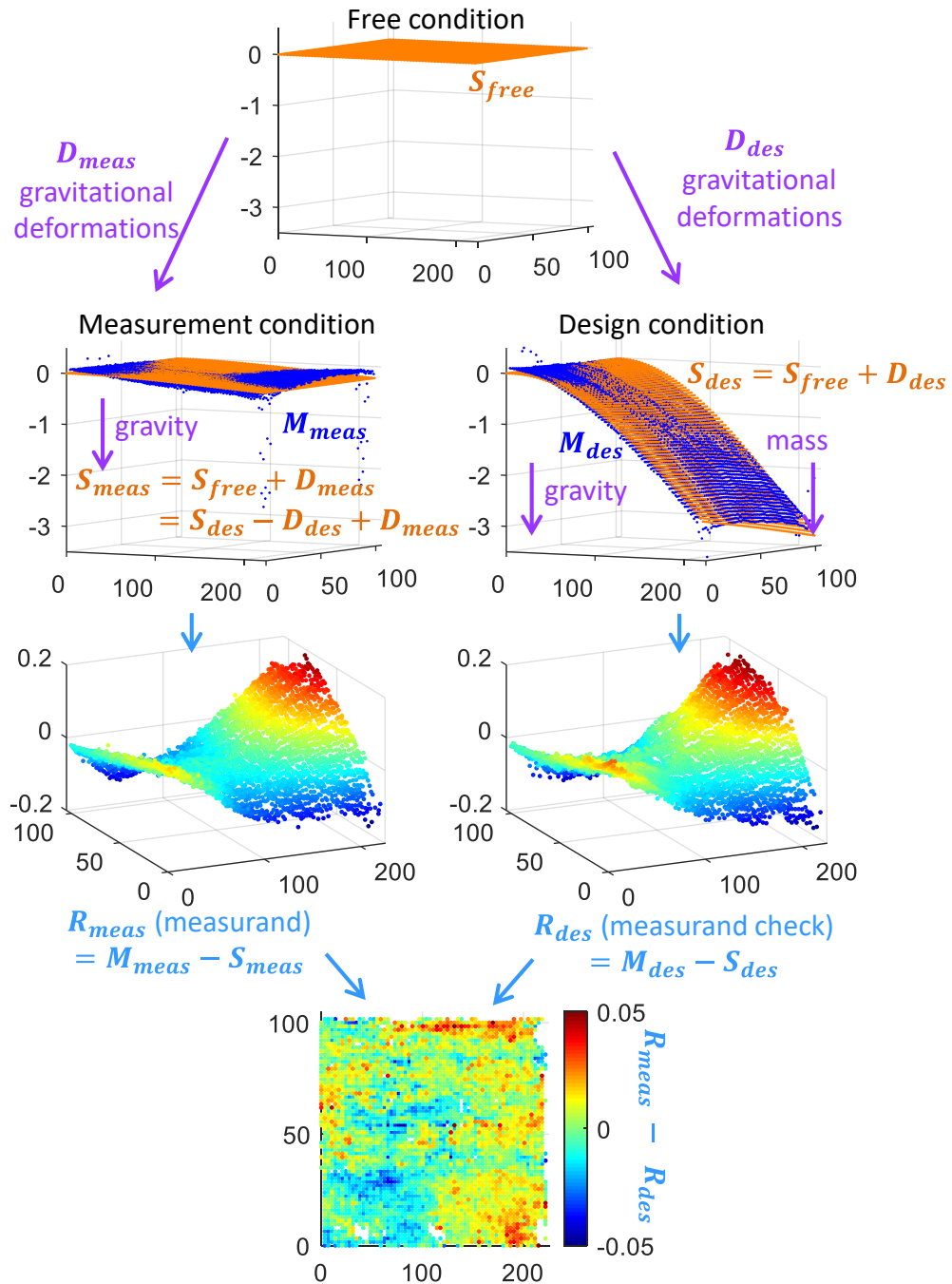
Figure 4-14: Review of cantilevered flat plate case study (units: mm)

CHAPTER 5: CANTILEVERED FLAT PLATE UNCERTAINTY ANALYSIS

This section seeks to understand which uncertainties are the main contributions to the ±25 μm mismatch between R_{meas} and R_{des} in the cantilevered flat plate case study.

The profile deviation calculation process involves FEA, point cloud registration, cylindrical searches, and so on. All of these steps are difficult to analyze through an uncertainty analysis because they cannot be represented in an analytical (i.e., closed form) expression. As such, a Monte Carlo style approach may be used. Monte Carlo uncertainty simulations involve generating a random set of input variables and repeatedly executing the calculation procedure to generate a set of outputs. The uncertainty can then be evaluated by analyzing the variation of the outputs. The software development for a complete Monte Carlo uncertainty simulation of the profile deviation calculation would be quite challenging considering the many software modules that must be automatically tied together for the analysis (Abaqus and many MATLAB® scripts). Also, the simulation would take hours of CPU time.

Given the challenges of the Monte Carlo method, a simplified uncertainty analysis is performed using beam theory as an approximation of the FEA. This uncertainty analysis only considers the effects of uncertainty in the FE inputs and point clouds. Uncertainties in the FE mesh, FE modeling errors, point cloud registration, environment, etc. will not be considered. Beam theory provides a closed form expression for the deflections of the plate which enables a GUM [14] based uncertainty analysis.

5.1. Closed form expression for profile deviations

The first step in a GUM [14] based uncertainty analysis is to mathematically express the relationship between the measurand (R_{meas}) and the input quantities.

Combining Equation (2.3) and (2.4), R_{meas} is represented in Equation (5.1). Allow D_g to represent the deformations due to gravity acting on the cantilevered plate such that it represents deformations from the weight of the plate itself. Allow D_M to represent the deformations due to the mass hanging on the cantilevered plate in the *design condition*. It follows that D_{meas} and D_{des} can be represented by Equation (5.2) and (5.3), respectively. Combining these equations, the simplified expression for R_{meas} is represented in Equation (5.4).

$$R_{meas} = M_{meas} - S_{des} + D_{des} - D_{meas} \tag{5.1}$$

$$D_{meas} = D_g \tag{5.2}$$

$$D_{des} = D_g + D_M \tag{5.3}$$

$$R_{meas} = M_{meas} - S_{des} + D_g + D_M - D_g \tag{5.4}$$

$$= M_{meas} - S_{des} + D_M$$

The cantilevered flat plate deflections from the mass (D_M) are approximated as a cantilever beam with a concentrated load at the end. Beer et al. [38] use beam theory to derive Equation (5.5) which represents the z deflections in the Figure 5-1 loading. For a beam of rectangular cross section, the second moment of area is calculated using Equation (5.6).

$$D_M = \frac{P}{6EI}(x^3 - 3Lx^2) = \frac{2Mg}{Ebt^3}(x^3 - 3Lx^2) \tag{5.5}$$

$$I = \frac{bt^3}{12} \tag{5.6}$$
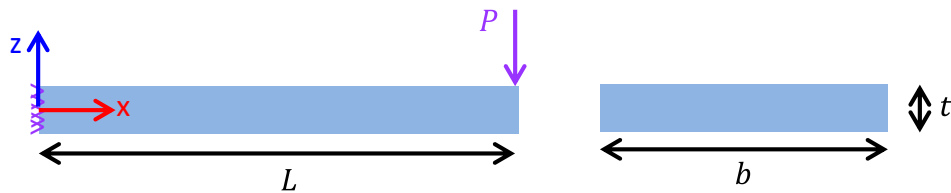
Figure 5-1: Concentrated load on a cantilever beam (inspired by Beer et al. [38])

The cantilevered flat plate deflections from its own weight (D_g) are approximated as a cantilever beam with a distributed load. Beer et al. [38] use beam theory to derive Equation (5.7) which represents the z deflections in the Figure 5-2 loading. The distributed load due to gravity is calculated using Equation (5.8).

$$D_g = -\frac{\omega}{24EI}(x^4 - 4Lx^3 + 6L^2x^2) = -\frac{\rho g}{2Et^2}(x^4 - 4Lx^3 + 6L^2x^2) \qquad (5.7)$$

$$\omega = \rho gbt \qquad (5.8)$$
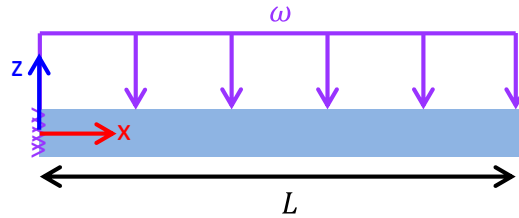
Figure 5-2: Distributed load on a cantilever beam (inspired by Beer et al. [38])

In Figure 5-3, the *design condition* (S_{des}) shape output from FEA is compared to the beam theory prediction of $S_{free} + D_g + D_M$. The beam theory mostly over-predicts the gravitational sag in comparison the FE model. They differ by a maximum of 0.45 mm (14% of total deflection) at x = 220 mm, y = 0 mm. The difference is expected considering the beam theory evenly distributes the concentrated force due to the mass along the x = 220 mm edge. Beam theory is also less accurate when the deflections (max around 3 mm in this case) are of the same order of magnitude as the thickness (2.479 mm). That is, the beam theory model performs better when the deflections are much less than the cross-sectional dimensions.

The 14% maximum difference between the FEA and beam theory predicted deflections is considered acceptable and the beam theory model will be used for the uncertainty analysis sensitivity coefficients. If anything, the beam theory conservatively overestimates the uncertainty.
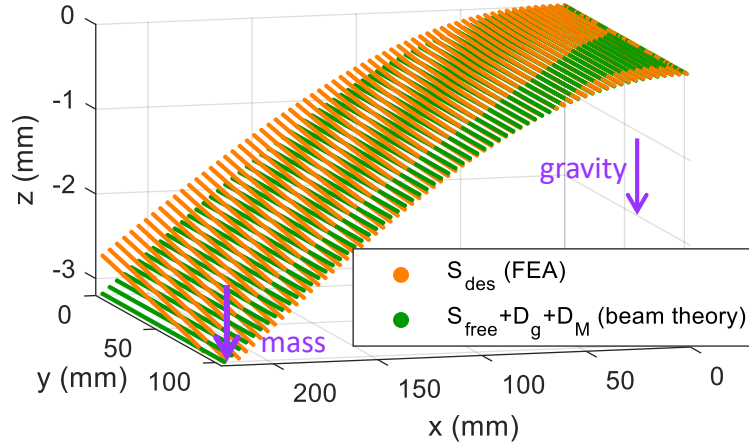
Figure 5-3: FEA versus beam theory predictions *design condition*

Finally, the closed form expression for $\boldsymbol{R_{meas}}$ is represented in Equation (5.9) by combining Equation (5.4) and (5.5).

$$\boldsymbol{R_{meas}} = \boldsymbol{M_{meas}} - \boldsymbol{S_{des}} + \frac{2Mg}{Ebt^3}(\boldsymbol{x}^3 - 3L\boldsymbol{x}^2) \tag{5.9}$$

5.2. Standard uncertainties

With a closed form expression for the measurand (Equation (5.9)) established, the next step in a GUM [14] based uncertainty analysis is to estimate a value for each input quantity and evaluate the standard uncertainty of each estimate, as presented in Table 5-1. Most of the standard uncertainties were evaluated by Type B methods, meaning statistical methods were not implemented. Table 5-1 provides comments on the details of the standard uncertainty calculation for each input quantity.

The estimated value for gravity was calculated using the Department of Defense World Geodetic System (WGS) of 1984 [39]. Geodetic systems involve the definition of three surfaces including the Earth's topographic surface (highly irregular, includes landmasses and ocean floor topography), a mathematical reference surface called an ellipsoid, and an equipotential surface called a geoid. The geoid is the equipotential surface associated with the mean ocean surface.

The gravity on the surface of the WGS84 ellipsoid can be calculated using Equation (5.10) (Equation 4-1 from [39]). With Duke Centennial Hall at UNC Charlotte (the building where experiments in this thesis were completed) having a latitude of 35.312°, the gravity was calculated as 9.7976 m/s^2.

$$g = g_e \frac{1 + k\,sin(\varphi)^2}{\sqrt{1 - e^2\,sin(\varphi)^2}} \tag{5.10}$$

$$g_e = 9.7803253359\ m/s^2$$

$$k = 0.00193185265241$$

$$e = 8.1819190842622\ x\ 10^{-2}$$

$$\varphi = geodetic\ latitude$$

The geoid reference surface for sea level is about 40 meters below the WGS84 ellipsoid near North Carolina (see Figure 6.1 from [39]). Charlotte then has an elevation from the geoid of about 180 meters, or 140 meters (180 m – 40 m) from the WGS84 ellipsoid. The vertical gravitational gradient is about -0.3x10^{-5} m/s^2/m [40]. Therefore, from elevation, the gravity in Charlotte is about 0.0004 m/s^2 (140*0.3x10^{-5}) lower than the WGS84 ellipsoid value. Additionally, gravity anomalies due to variations in the density of the Earth's crust are typically around 0.0005 m/s^2 [41]. With the elevation and crust density effects considered, a standard uncertainty of 0.001 m/s^2 seemed reasonable to account for these anomalies.

The other standard uncertainty calculations were much simpler and are provided in Table 5-1.

Table 5-1: Estimated values and standard uncertaitnies of input quanitites

Input quantity	Units	Est. value	Stand. uncert.	Type	Estimated value source	Standard uncertainty calculation comments
M_{meas} M_{des}	point clouds	mm	N/A	0.018	B	ROMER Arm scanner	Spec sheet RS4 scanning system accuracy is 0.063 mm, assuming rectangular distribution of 0.063 mm full width, u = 0.063 mm/sqrt(12)
M	mass	kg	0.7398	0.0001	B	Ohaus Adventurer Pro AV4101	Spec sheet 1σ
g	gravity	m/s^2	9.7976	0.001	B	Equation (5.10)	Estimated normal distribution 1σ based off Bouguer anomolies and vertical gravity gradients
E	modulus of elasticity	N/mm^2	69x10^3	0.5x10^3	B	MatWeb online materials database	Estimated normal distribution 1σ to cover range of aluminum alloys with density between 2.68 and 2.72 g/cm^3 in MatWeb database
b	width	mm	101.63	0.022	B	ROMER Arm touch probe	Spec sheet volumetric accuracy is 0.038 mm, assuming rectangular distribution of 0.038 mm half width, u = 0.038 mm/sqrt(3)
t	thickness	mm	2.479	0.011	A	Aerospace micrometers	Standard deviation of 8 measurements / sqrt(8)
L	length	mm	221.68	0.022	B	ROMER Arm touch probe	Spec sheet volumetric accuracy is 0.038 mm, assuming rectangular distribution of 0.038 mm half width, u = 0.038 mm/sqrt(3)

5.3. Combined standard uncertainty

As described in the GUM [14], in order to calculate a combined standard

uncertainty (u_c) for R_{meas} the standard uncertainties of each input (Table 5-1) must be

propagated through the closed form relationship ($Y = f(X_1, X_2, ..., X_N)$) using Equation

(5.11). Note, here i represents the index into the number of input quantities N which are

both unrelated to their meaning in the profile deviation calculation.

$$u_c^2(Y) = \sum_{i=1}^{N} \left(\frac{\partial f}{\partial X_i}\right)^2 u^2(X_i) \tag{5.11}$$

The partial derivatives of the closed form R_{meas} (Equation (5.9)) used to evaluate

Equation (5.11) are listed in Equation (5.12) through (5.19).

$$\frac{\partial R_{meas}}{\partial M_{meas}} = 1 \tag{5.12}$$

$$\frac{\partial R_{meas}}{\partial S_{des}} = -1 \tag{5.13}$$

$$\frac{\partial R_{meas}}{\partial M} = \frac{2g}{Ebt^3}(x^3 - 3Lx^2) \tag{5.14}$$

$$\frac{\partial R_{meas}}{\partial g} = \frac{2M}{Ebt^3}(x^3 - 3Lx^2) \tag{5.15}$$

$$\frac{\partial R_{meas}}{\partial E} = -\frac{2Mg}{E^2bt^3}(x^3 - 3Lx^2) \tag{5.16}$$

$$\frac{\partial R_{meas}}{\partial b} = -\frac{2Mg}{Eb^2t^3}(x^3 - 3Lx^2) \tag{5.17}$$

$$\frac{\partial R_{meas}}{\partial t} = -\frac{6Mg}{Ebt^4}(x^3 - 3Lx^2) \tag{5.18}$$

$$\frac{\partial R_{meas}}{\partial L} = -\frac{2Mg}{Ebt^3}(3x^2) \tag{5.19}$$

Finally, the combined standard uncertainty of R_{meas} can be evaluated as provided

in Table 5-2. Since the sensitivity coefficients are a function of x, it is expected that the

uncertainty contribution from D_M (recall Equation (5.4)) will be 0 at $x = 0$ and increase

to a maximum at $x = L$. As such, the sensitivity coefficients were evaluated at $x = L$ to

attain the maximum uncertainty. S_{des} was considered to have no uncertainty since it is

the surface defined by the designer.

The combined uncertainty for R_{meas} at $x = L$ came to 0.048 mm. The only

contributions over 1 µm came from M_{meas}, E, and t. Improvement in the M_{meas}

contribution would likely require using a different scanner or a study specifically to characterize the performance of the ROMER Arm RS4 scanner. Improvement in the E contribution should be simple in an industrial setting as the manufacturer would likely be more knowledgeable about the properties of the material they were using. The largest contributor came from the 0.011 mm uncertainty in the thickness for a contribution of 0.039 mm. This contribution is challenging to improve upon given that it is limited by the thickness variation throughout the plate. Improving the thickness contribution would require adjusting the manufacturing process to attain greater thickness uniformity.

Table 5-2: Combined standard uncertainty of $\boldsymbol{R_{meas}}$ at $x = L$

Input quantity X_i		Standard uncertainty $u(X_i)$		Sensitivity $\frac{\partial R_{meas}(x = L)}{\partial X_i}$		Contribution (mm) $u(X_i)\left\|\frac{\partial R_{meas}}{\partial X_i}\right\|$
$\boldsymbol{M_{meas}}$	point cloud	0.018	mm	1	mm/mm	0.0182
$\boldsymbol{S_{des}}$	CAD	0	mm	-1	mm/mm	0.0000
M	mass	0.0001	kg	-4.0	mm/kg	0.0004
g	gravity	0.001	m/s^2	-0.30	mm/(m/s^2)	0.0003
E	modulus of elasticity	0.5x10^3	N/mm^2	4.3x10^{-5}	mm/(N/mm^2)	0.0214
b	width	0.022	mm	0.029	mm/mm	0.0006
t	thickness	0.011	mm	3.6	mm/mm	0.0394
L	length	0.022	mm	-0.020	mm/mm	0.0004

$$u_c\big(R_{meas}(x = L)\big) = \sqrt{\textstyle\sum_{i=1}^{N}\left(\frac{\partial R_{meas}(x=L)}{\partial X_i}\right)^2 u^2(X_i)} = \quad 0.048$$

The $\boldsymbol{M_{meas}}$ scanner uncertainty is expected to be randomly distributed while uncertainties in material properties (Table 5-2 less $\boldsymbol{M_{meas}}$ and $\boldsymbol{S_{des}}$) increase towards the free end of the plate. The uncertainty contributions from the material properties increase as a function of x in Figure 5-4. In contrast, the $\boldsymbol{M_{meas}}$ scanner uncertainty contribution is spatially invariant over the plate.
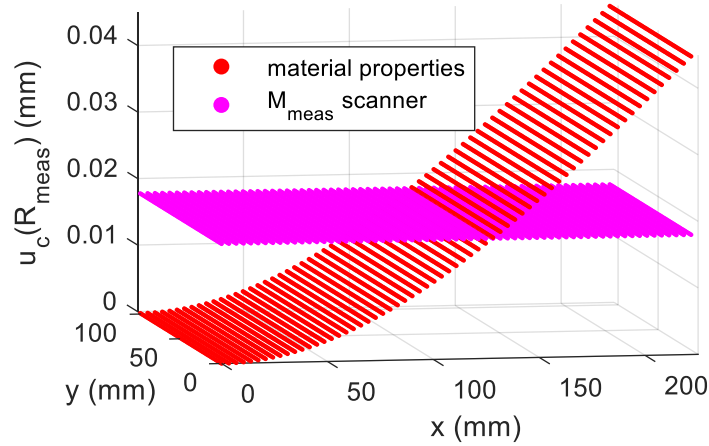
Figure 5-4: Contributions from the material properties and scanner to the combined standard uncertainty in R_{meas}

Recalling Equation (2.5), the profile deviation measured in the *design condition* (measurand check) is calculated as $R_{des} = M_{des} - S_{des}$. From Table 5-2, S_{des} has no uncertainty so the uncertainty in the *design condition* profile deviation is simply $u_c(R_{des}) = u_c(M_{des})$ which is 0.018 mm (recall Table 5-1).

The $u_c(R_{des})$ of 0.018 mm and $u_c(R_{meas}(x = L))$ of 0.048 mm are consistent with the case study results (95% of $R_{meas} - R_{des}$ within ±25 µm, Table 4-2). The best fit registration operations help to remove some of the uncertainties due to material properties (Figure 5-4).

CHAPTER 6: PROPOSED APPROACH UPDATE

The proposed approach outlined in Chapter 2 worked well for the cantilevered plate (Chapter 4). However, the cantilever plate was statically determinate such the reaction forces in the FE simulations (defect-free plate) matched those in reality (profile deviation laden plate). When the FE simulations were completed to calculate gravitationally induced sag (Figure 4-5), the reaction forces in both FEA and in the real measurement were equal to the weight of the plate (*measurement condition*) or the weight of the plate and mass (*design condition*).

In the following section, the proposed approach is applied to a statically indeterminate case. The proposed approach in its Chapter 2 form is shown to be inadequate (R_{meas} does not match R_{des}) and updates are introduced to address the inadequacies.

6.1. Consequences of over-constrained design conditions

Consider a flat plate 200 mm x 100 mm x 0.25 mm in size with the same aluminum density, modulus of elasticity, and Poisson's ratio used with the cantilevered plate (section 4.2). It is clamped to 4 planar locators in the *design condition* and simply supported on 3 locators in the *measurement condition*, as shown in Figure 6-1. M1, M2, and M3 represent the *measurement condition* locators while D1, D2, D3, and D4 represent the *design condition* locators.
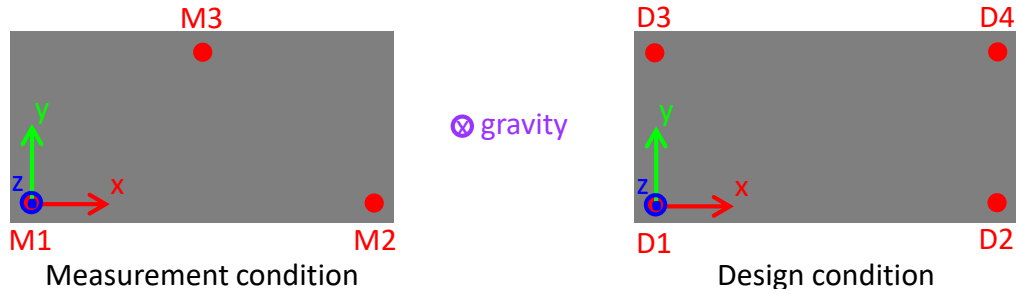
Figure 6-1: Flat plate *measurement* and *design condition* inspection fixtures

This case differs from the cantilevered plate case in that the *design condition* is statically indeterminate.

Let F_{M1}, F_{M2}, and F_{M3} be the reaction forces in the z direction at the *measurement condition* locators. Assuming forces in the y and z direction are negligible, the static equilibrium equations available are $\sum F_z = 0$, $\sum M_x = 0$, and $\sum M_y = 0$. With F_{M1}, F_{M2}, and F_{M3} as the only unknowns, there are 3 equations and 3 unknowns allowing the *measurement condition* reaction forces to be directly solved for. Now, superimpose any reasonable profile deviation field (maximum of around 1 mm, perhaps) on the nominally flat plate. This will negligibly change the position of the center of gravity and thus the reaction forces will be negligibly changed.

Let F_{D1}, F_{D2}, F_{D3}, and F_{D4} be the reaction forces in the z direction at the *design condition* locators. Again, the static equilibrium equations available are $\sum F_z = 0$, $\sum M_x = 0$, and $\sum M_y = 0$. There are now 3 equations and 4 unknowns preventing the *design condition* reaction forces from being solved for directly. Given that the plate is nominally flat and the clamps are equally spaced about the center of gravity, the reaction forces at each clamp will simply be a fourth of the weight of the plate. FE simulations of the *design condition* agree with this conclusion and show reaction forces equal to a fourth of the plate weight at each clamp (see Figure 6-3b in the next section).

As in the *measurement condition* thought experiment, superimpose the same profile deviation field on the nominally flat plate and the center of gravity is negligibly affected. However, the over-constrained *design condition* now has the ability to remove a component of the profile deviation field by forcing the 4 corners to be planar. A component of the profile deviation field is therefore removed which also causes the reaction forces to be redistributed (see Figure 6-4b in the next section). This situation will be examined through a hypothetical case study in the next section.

6.2. Case study - Saddle plate

This section applies the proposed approach to the flat plate case previously described in Figure 6-1. The challenge of the over-constrained (i.e., statically indeterminate) *design condition* is revealed. The case study uses purely simulated data. That is, the measured point clouds were artificially generated.

The nominally flat plate (in zero gravity) was meshed with a 64 element x 64 element quad shell mesh resulting in 4096 elements and 4225 nodes. Two FE simulations were completed to produce the hypothetical profile deviation field. The hypothetical profile deviation consisted of a) a saddle component capable of being removed by the *design condition* fixture and b) a bow component incapable of being removed by the *design condition* fixture.

The saddle shape was generated by displacing the fourth locator (D4) of the *design condition* -2 mm in z. The resulting shape and vertical reaction forces at each clamp are shown in Figure 6-2a. The bow component was generated by displacing the node at x = 0 mm, y = 50 mm 1 mm in z while constraining the four clamp locations. The resulting shape is shown in Figure 6-2b. The Figure 6-2b component cannot be removed

by the *design condition* because the 4 locators are already planar. On the other hand, Figure 6-2a can be removed because D4 will force the fourth corner into plane at z = 0, removing the saddle.
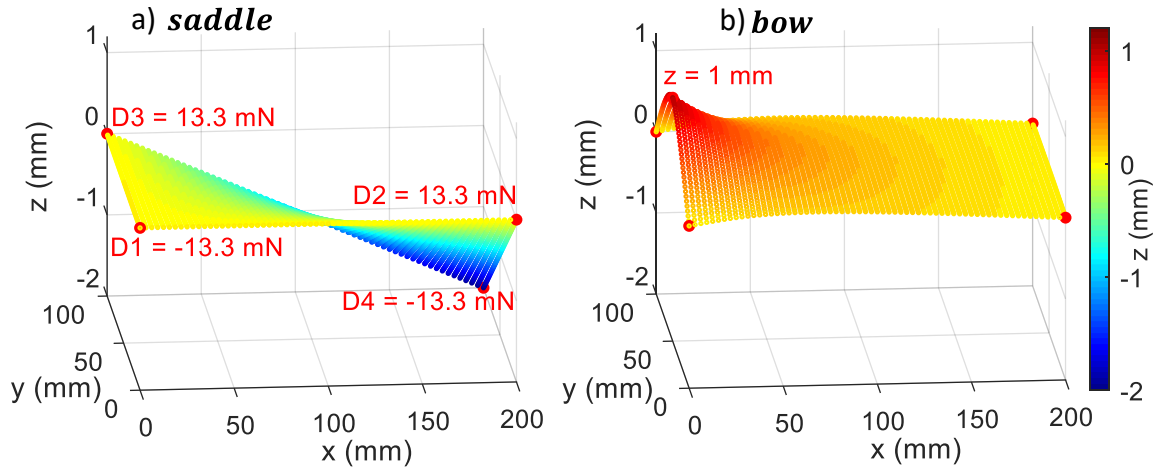
Figure 6-2: a) saddle component and b) bow component of hypothetical profile deviation

In accordance with the Figure 2-4 performance check, gravity was applied in FEA to predict the defect-free surfaces in the *measurement* and *design conditions* as shown in Figure 6-3. Notice in Figure 6-3b that the FEA predicted reaction forces are equally distributed because this represents the defect-free plate (no profile deviations).
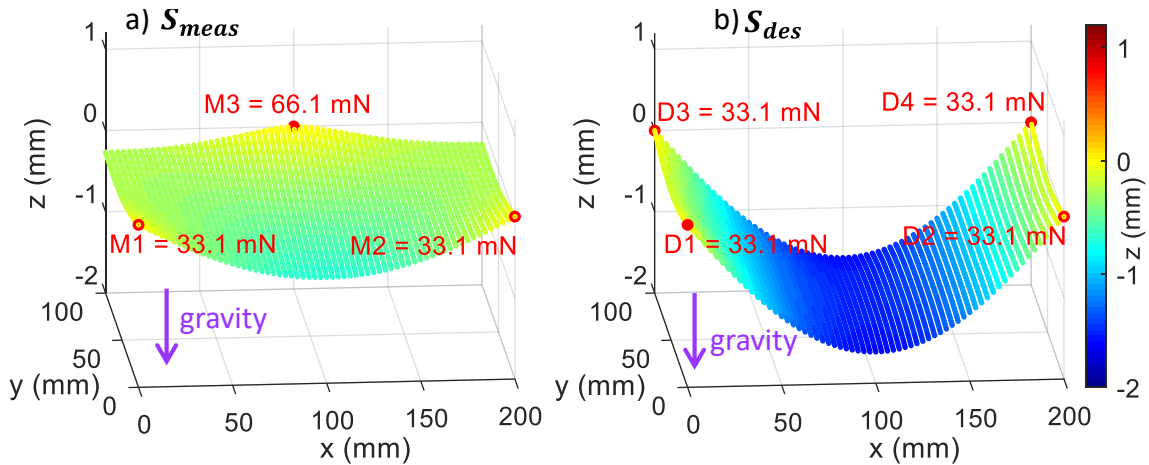
Figure 6-3: Defect-free flat plate under the influence of gravity in the a) *measurement condition* and b) *design condition*. Reaction forces represent predicted forces in the fixtures when supporting the nominal defect free part.

Next, the hypothetical profile deviations were used to create measured point clouds which contain the profile defects. The *measurement condition* point cloud ($\boldsymbol{M_{meas}}$) was created by adding $\boldsymbol{saddle}$ and $\boldsymbol{bow}$ to $\boldsymbol{S_{meas}}$. Both components ($\boldsymbol{saddle}$ and $\boldsymbol{bow}$) of the profile deviation show up in the *measurement condition* because the 3 support measurement fixture is statically determinate and does not have the ability to remove either component. The reaction forces of $\boldsymbol{M_{meas}}$ are the same as $\boldsymbol{S_{meas}}$ because profile deviations negligibly effect statically determinate reaction forces. $\boldsymbol{M_{meas}}$ is shown in Figure 6-4a.

The *design condition* point cloud ($\boldsymbol{M_{des}}$) was created by adding $\boldsymbol{bow}$ to $\boldsymbol{S_{des}}$. Only the $\boldsymbol{bow}$ component of the profile deviation shows up in the *design condition* because the 4 clamp design fixture has the ability to remove the $\boldsymbol{saddle}$ component. The reaction forces of $\boldsymbol{M_{des}}$ are equal to $\boldsymbol{S_{des}}$ reaction forces minus $\boldsymbol{saddle}$ reaction forces because the four clamps must overcome the saddle shape and force the four corners into plane. $\boldsymbol{M_{des}}$ is shown in Figure 6-4b.This illustrates the concept from section 6.1 that profile deviations redistribute reaction forces in over-constrained statically indeterminate fixtures.
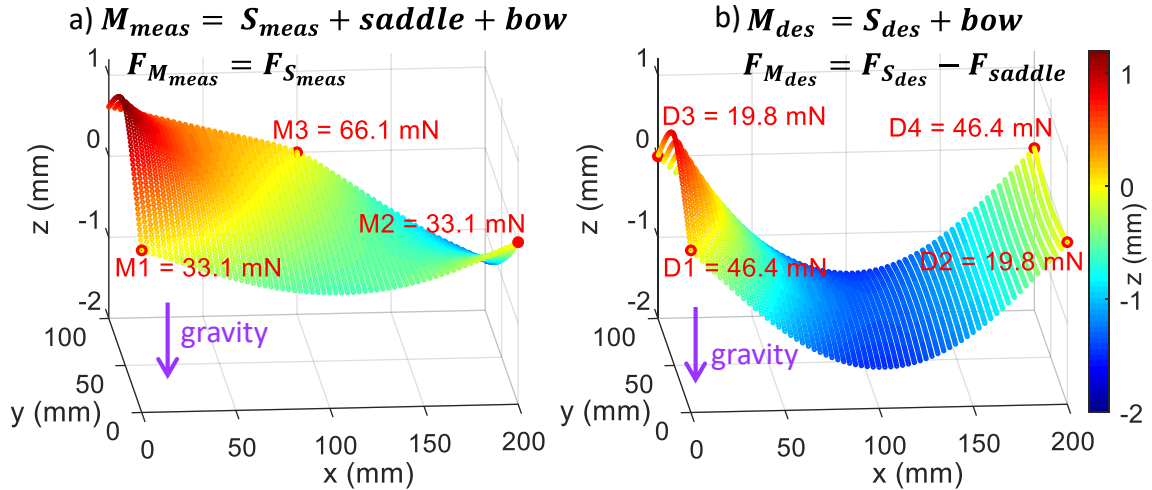
Figure 6-4: Hypothetical point clouds in the a) *measurement condition* and b) *design condition*, reaction forces represent "real" forces in the fixtures when measuring the "real" defect laden part. Quotation marks are added to "real" as a reminder that the measured point clouds with profile deviations were artificially generated.

Finally, the profile deviations were directly evaluated with Equation (2.4) and (2.5). Point cloud processing from section 2.2 was not required because the artificially generated point clouds are represented as deformed FE meshes. The results are shown in Figure 6-5. Recall that the proposed approach is judged by how closely R_{meas} and R_{des} match. They clearly do not match.
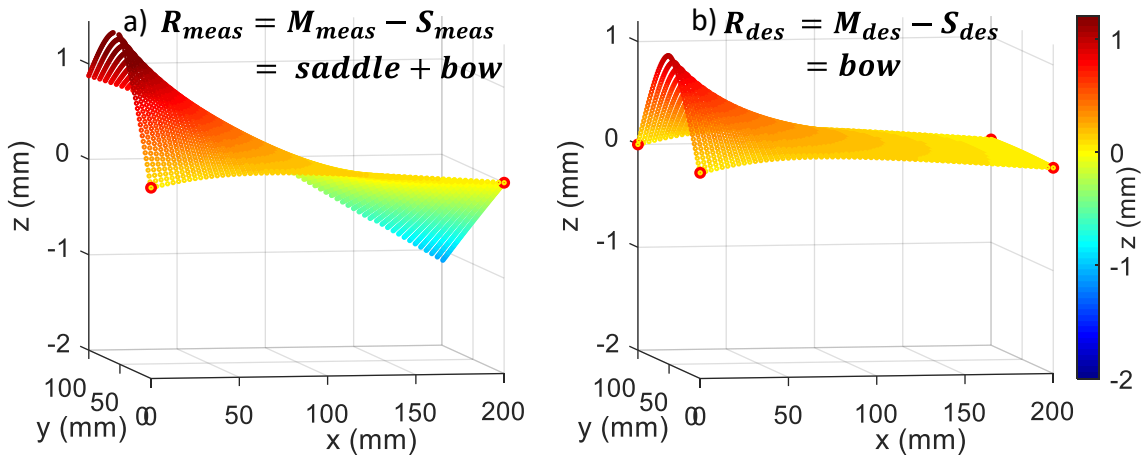
Figure 6-5: Hypothetical measured profile deviations in the a) *measurement condition* and b) *design condition*

53

This case study on a flat plate with saddle profile deviations revealed two improvements required to apply the proposed approach to over-constrained statically indeterminate *design conditions*.

First, as shown in Figure 6-5, the profile deviation predicted from the proposed approach (R_{meas}) did not match the common industry practice of the *restrained on a shaped fixture* approach (R_{des}). The difference between R_{meas} and R_{des} is simply the saddle shape from Figure 6-2a because the *design condition* fixture removes the saddle shape by forcing the four corners into plane. In contrast, the *measurement condition* fixture has no mechanism to remove the saddle. The proposed approach must be updated to account for "mode" shapes that the *design condition* fixture is capable of removing.

Second, in some industrial cases (see for example, Abenhaim et al. [22]), to guarantee a person is strong enough to assemble a component, the designer places limits on the allowable forces to push the part into its *design condition* (i.e., in this case, the force required to make the four corners of the plate planar in the *design condition*). The proposed approach in its Chapter 2 form does not provide a means to predict the assembly forces (i.e., reaction forces). According to the proposed approach, the assembly forces in the *design condition* are equally distributed (S_{des}, Figure 6-3b) regardless of the profile deviation. In reality, Figure 6-4b demonstrated that the reaction forces are strongly influenced by the profile deviation. Prediction of the assembly forces will increase the industrial applicability of the proposed approach

For completeness, the saddle plate case study is summarized in Figure 6-6 (analogous to Figure 2-4 and Figure 4-14).
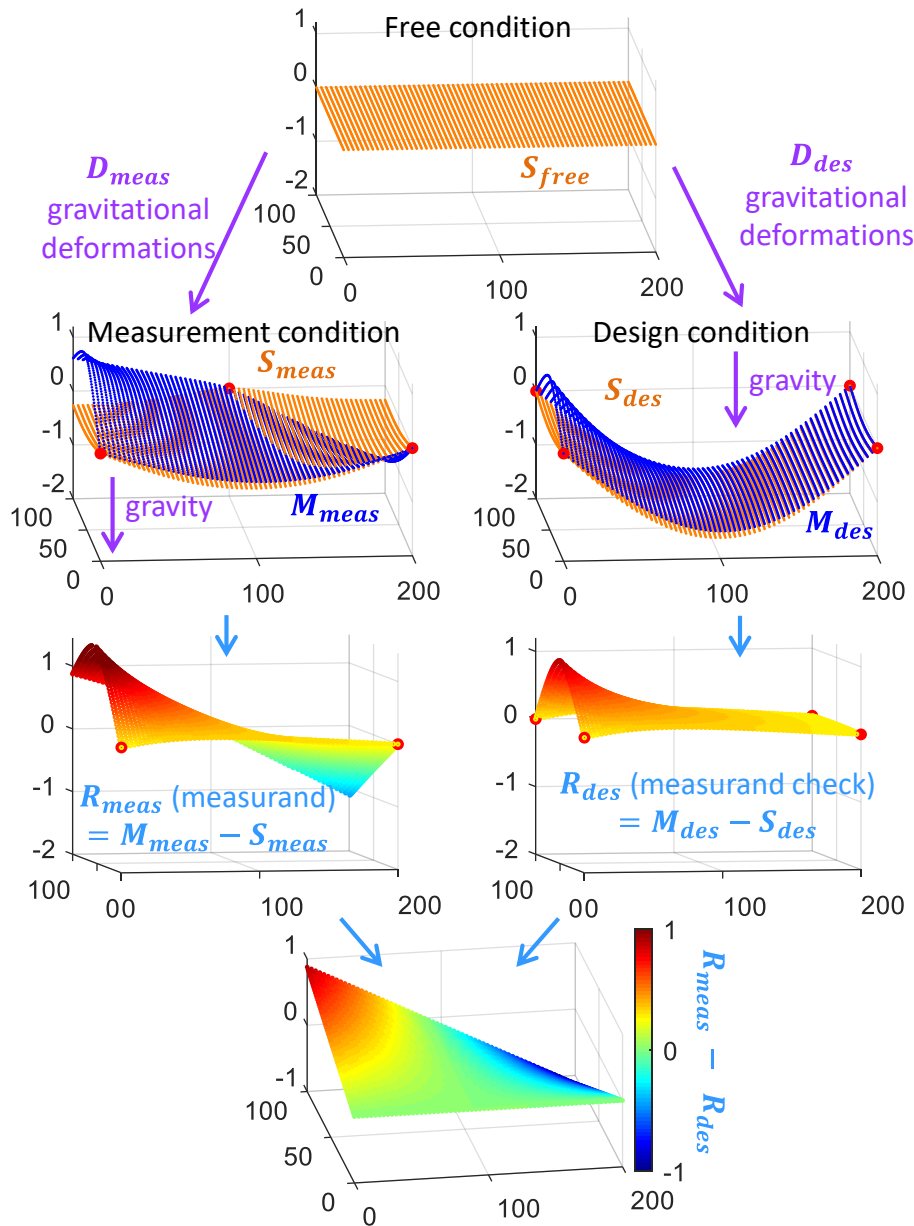
Figure 6-6: Review of saddle plate case study (units: mm)

6.3. Proposed approach update

This section updates the profile deviation calculation from section 2.2 to address the two shortcomings mentioned in the previous section. That is, 1) correct $\boldsymbol{R_{meas}}$ for "mode" shapes the *design condition* fixture is capable of removing and 2) provide a means to calculate the assembly forces that deform the real defect-laden part into the *design condition*. Quotation marks are added to "mode" to notify the reader that the

definition differs from the way "mode" is commonly used to describe vibrations in structures.

These shortcomings could be addressed by virtually assembling the measured part to the *design condition* fixture. That is, by taking *the measurement condition* point cloud (M_{meas}), correcting it for gravitational sag, rigidly aligning it to three of the *design condition* locators (recall Figure 6-1 D1, D2, and D3 locators), and removing mode shapes from the measured point cloud such that it touched the fourth *design condition* locator (D4). The transformed and mode shape adjusted M_{meas} could then be compared to S_{des} to evaluate the profile deviation. The assembly forces could be calculated form the magnitude of the mode shape removal. This technique would work, however it involves processing the measured point cloud from the *measurement condition* to the *design condition*. This should be avoided because computations involving the point clouds (M_{des}, M_{meas}) are expensive. The point clouds contain 10 to 100 times more data points that the mesh representing the CAD model (S_{des}, S_{meas}).

The previous paragraph was included to provide the simplest conceptual understanding for evaluating the profile deviation using mode shape removal. The proposed approach update implements this concept essentially in reverse by taking the *design condition* CAD to the *measurement condition* scan data, as initially described in Figure 2-1.

The updated proposed approach adjusts the measurement condition CAD model (S_{meas}) with the mode shapes, calculates the assembly forces, then evaluates the point cloud (S_{meas}) against the adjusted S_{meas} to calculate the profile deviation (R_{meas}) using the steps

from section 2.2. The step by step procedure for the profile deviation and assembly force

calculation is as follows:

1) Use FEA to predict the deflections due to *design condition* ($\boldsymbol{D_{des}}$) and

   measurement condition ($\boldsymbol{D_{meas}}$) gravitational loads. Use Equation (2.3) to

   calculate the *measurement condition* defect-free geometry $\boldsymbol{S_{meas}}$. Store the defect-

   free *design condition* reaction forces predicted from the $\boldsymbol{D_{des}}$ simulation in $\mathbf{F_{S_{des}}}$.

2) Use FEA to predict the mode shapes $\boldsymbol{V_r}$ that the *design condition* fixture is

   capable of removing.

   a. Identify 3 locators in the *design condition* which will be used to define the

      design condition coordinate system. These locators, D1, D2, and D3 will

      be considered *principal* locators. The remaining locators, D4, D…, will be

      considered *supplementary* locators. That is, they define the over-

      constraining locators that are capable of distorting the part and removing

      mode shapes.

   b. Perform FEA on the *design condition* CAD ($\boldsymbol{S_{des}}$) to predict the mode

      shapes the *supplementary* locators remove. Each mode shape is created by

      displacing the specific *supplementary* locator an arbitrary distance while

      constraining the other locators to zero displacement. Complete this for

      each *supplementary* locator creating a set of "modes" $\boldsymbol{V_r}$ that represent the

      shapes that can be removed (for the saddle plate, D4 is the only

      supplementary locator so the only mode is $\boldsymbol{V_{D4}}$). Each $\boldsymbol{V_r}$ (one for each

      supplementary locator mode), is an $mx3$ matrix containing the dXdYdZ

      displacement of each mesh node. Store the resulting reaction forces for

each mode V_r at each locator in F_{V_r} (e.g., $F_{V_{D4}}$ will contain the reaction

forces for D1, D2, D3, and D4 from V_{D4}).

3) Transform S_{meas} to contact the three *principal* locator (D1, D2, D3) positions on

M_{meas}, creating $S_{meas,T}$.

4) Scale and add the mode shapes to $S_{meas,T}$ to force it to contact the *supplementary*

locator (D4, D…) positions on M_{meas}. That is, find the coefficient C for each

mode shape to make $S_{meas,V}$ touch M_{meas} at the *supplementary* locator (D4, D…)

positions, where $S_{meas,V}$ is provided by Equation (6.1).

$$S_{meas,V} = S_{meas,T} + \sum_r C_r V_r \tag{6.1}$$

5) Use the coefficients C to predict the assembly forces F. The assembly forces are

calculated with Equation (6.2), where $F_{S_{des}}$ is the reaction force at each locator

output from the FEA simulation that produced D_{des} (recall Figure 6-3b).

$$F = F_{S_{des}} - \sum_r C_r F_{V_r} \tag{6.2}$$

6) Use Equation (6.3) to calculate the profile deviation field (measurand) R_{meas}.

This equation is evaluated using the point cloud processing steps from section 2.2.

$$R_{meas} = M_{meas} - S_{meas,V} \tag{6.3}$$

Steps 1) and 2) are "pre-processing" as they are only executed once per part

design. Steps 3) to 6) are "processing" as they must be executed for every single

measured part. Within the processing category, steps 3) to 5) involve CAD model

adjustment while step 6) processes the point cloud.

6.4. Saddle plate revisited

This section revisits the saddle plate case study by applying the proposed

approach update detailed in the previous section.

Applying step 1), $\boldsymbol{D}_{des}$ and *measurement condition* ($\boldsymbol{D}_{meas}$) were calculated through FEA by applying a gravitational load and restraining displacement at the locators. These data sets were combined with $\boldsymbol{S}_{des}$ to calculate the *measurement condition* defect-free geometry $\boldsymbol{S}_{meas}$, as previously shown in Figure 6-3.

Applying step 2), the *design condition* locators from Figure 6-1 were grouped into *principal* locators (D1, D2, and D3) and a *supplementary* locator (D4). $\boldsymbol{V}_{D4}$ was created by displacing D4 vertically 1 mm. The resulting shape and reaction forces are shown in Figure 6-7.
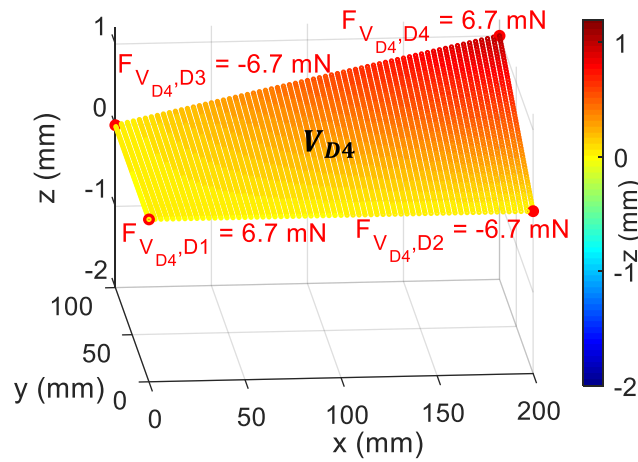
Figure 6-7: Saddle plate mode shape and reaction forces

Applying step 3), $\boldsymbol{S}_{meas}$ (previously shown in Figure 6-3a) was transformed to contact the D3 position of $\boldsymbol{M}_{meas}$ (previously shown in Figure 6-4a), creating $\boldsymbol{S}_{meas,T}$. Since the *measurement condition* and *design condition* both share the bottom corners as locators (recall Figure 6-1), $\boldsymbol{S}_{meas}$ was already in contact with $\boldsymbol{M}_{meas}$ at D1 and D2. The transformation is shown in Figure 6-8.
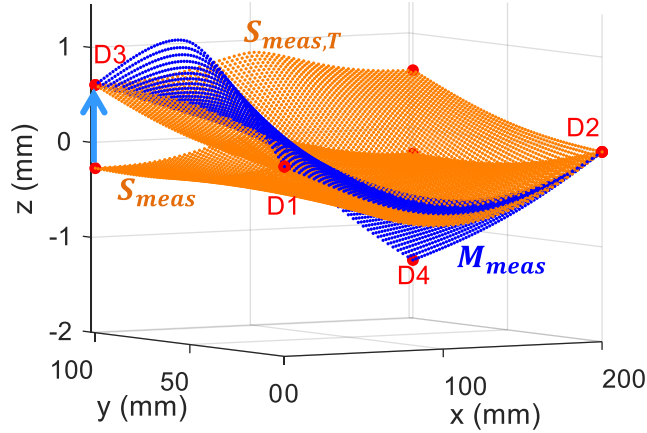
Figure 6-8: Transformation of S_{meas} to contact D3

Applying step 4), the coefficient C_{D4} was used to scale V_{D4} to adjust $S_{meas,T}$ such

that $S_{meas,V}$ contacted the D4 position of M_{meas}. Since the D4 position is x = 200 mm, y

= 100 mm, the calculation was simply $C_{D4} = \frac{M_{meas}(x=200,y=100) - S_{meas,T}(x=200,y=100)}{V_{D4}(x=200,y=100)}$

$= \frac{-1.389\ mm - 0.611\ mm}{1\ mm} = -2$. Applying Equation (6.1) the mode shape adjusted $S_{meas,V}$

is shown in Figure 6-9 to contact M_{meas} at all the locator positions.
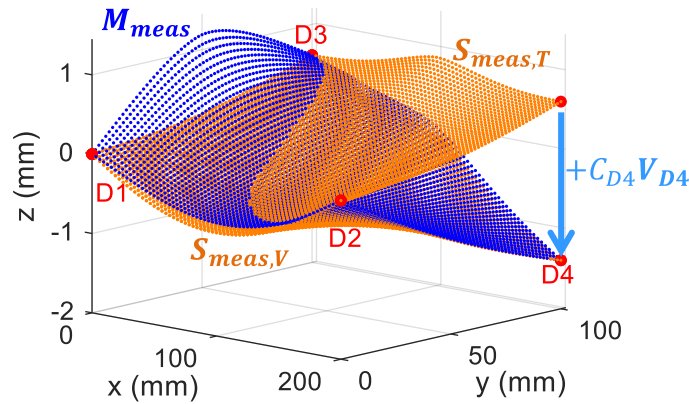
Figure 6-9: Mode shape adjusted S_{meas} to create D4 contact with M_{meas}

Applying step 6) and Equation (6.3), the profile deviation field adjusted for mode

shapes is presented in Figure 6-10. Applying step 5) and Equation (6.2) the assembly

forces were calculated and overlaid on Figure 6-10.

Comparing R_{meas} (Figure 6-10) to R_{des} (Figure 6-5b), they appear identical. This indicates that the updated proposed approach successfully removed the shapes that the *design condition* fixture is capable of removing. Also, the predicted assembly forces F (Figure 6-10) match the "real" forces (Figure 6-4b) in the *design condition* fixture when measuring the "real" defect laden part indicating the updated proposed approach is capable of predicting assembly forces. In this case, since all the reaction forces are positive that means they are pushing up on the plate and gravity took care of forcing contact at all locators. Negative assembly forces would indicate an external downward force (applied by a clamp, perhaps) would be required to create contact at all locators.

A summary of the updated approach applied to the saddle plate case study is provided in Figure 6-11. It is the updated version of Figure 6-6.
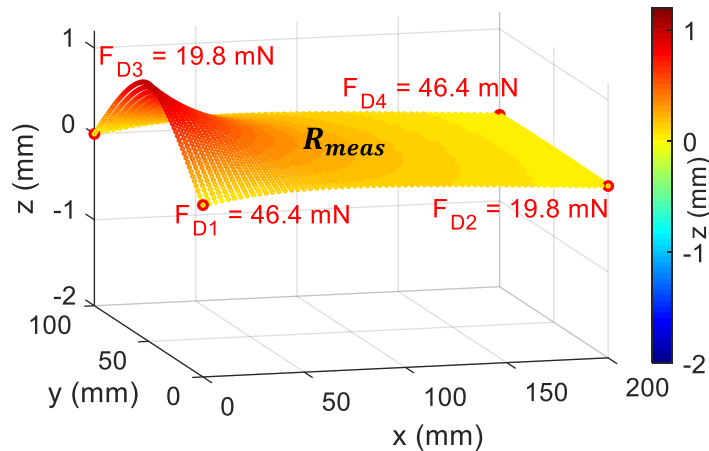
Figure 6-10: Profile deviation R_{meas} (measurand) and predicted assembly forces F from the updated proposed process

61
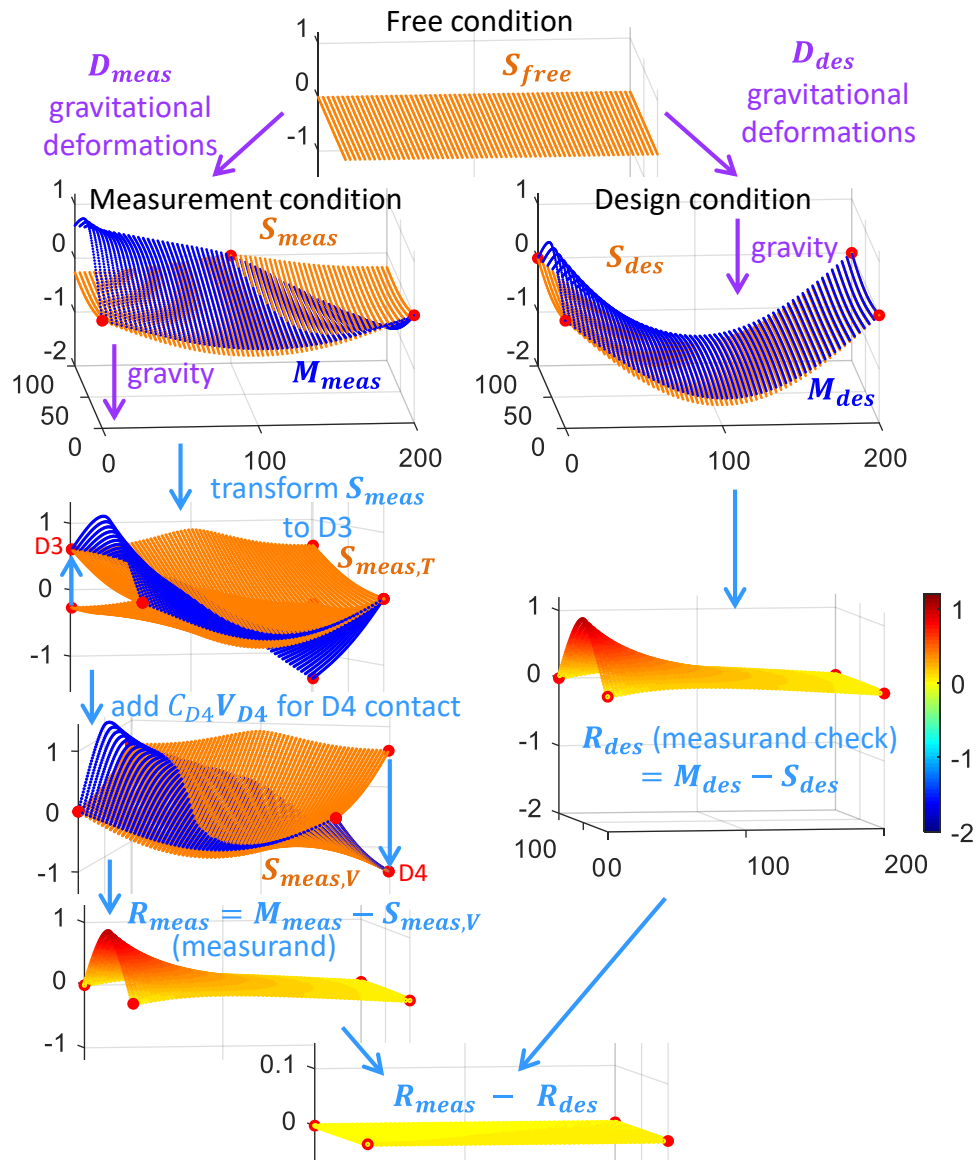
Figure 6-11: Review of updated saddle plate case study (units: mm)

CHAPTER 7: CASE STUDY - AUTOMOTIVE FENDER

The saddle plate case study provided a conceptual method for overcoming the challenges of over-constrained *design conditions*. To put the updated proposed approach to the test on an industrially relevant part, the following chapter applies it to the fixtureless inspection of an automotive fender. The fender used in this case study was a repair section from the rear body panel of a 1973 British Motor Company MGB, as shown in Figure 7-1.
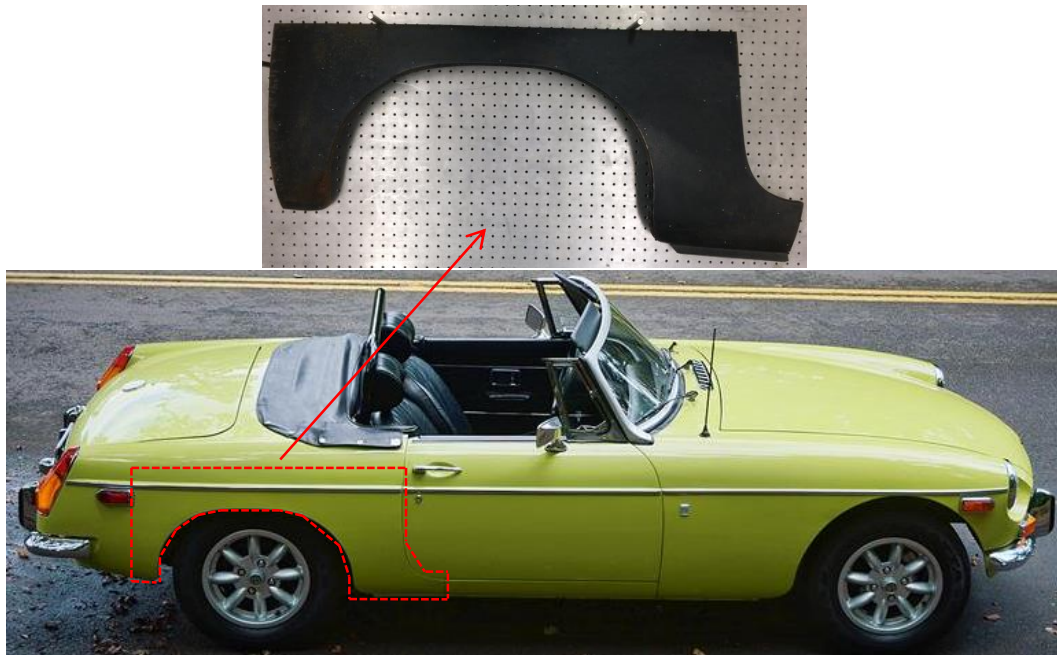
Figure 7-1: 1973 MGB rear fender section (source: sportscarshop.com/yellow-mgb/)

The *design condition* was defined as clamped to eight locators on a table top and was intended to mimic the fender to vehicle attachment locations. The table top had ¼"-20 holes spaced in a 1" by 1" grid. The eight locators were constructed out of 1" diameter spheres mounted on standoffs ranging from 1" to 2.5" in height. The locators were labeled D1 through D8 as shown in Figure 7-2b. The coordinate system was constructed with the x-y plane through the D1, D2, and D3 sphere centers. The x axis was parallel to

a line through D2 and D3 and the origin was position at D1. X1, Y1, and Y2 were

cylinders used to horizontally locate the fender in the fixture during measurement. Figure

7-2d shows the right fender clamped in the *design condition* fixture.

The *measurement condition* was defined as lying on a table top with just a small

support in the middle (M2) to create a statically determinate three-point support as shown

in Figure 7-2a. The fender in the fixtureless measurement condition along with the three

contact points M1, M2, and M3 is shown in Figure 7-2c.
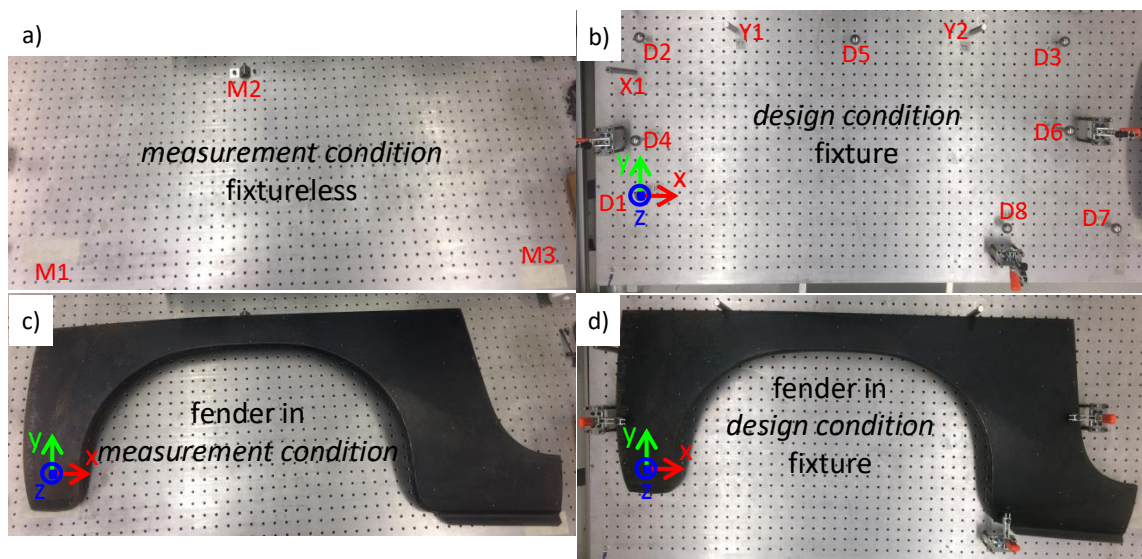
Figure 7-2: a) fixtureless *measurement condition*, b) *design condition* fixture, c) fender in
the *measurement condition*, and d) fender in the *design condition*

7.1. CAD creation from L fender

Since CAD data for a classic vehicle is difficult to attain, the CAD model was

created out of scan data. The results would not be very interesting if the right fender was

used to create the CAD model and then the right fender was inspected, as the profile

deviations should be zero. Instead, the CAD model was generated out of the L (left)

fender and mirrored to represent the right fender.

A *design condition* fixture for the L fender was constructed by mirroring all the locators over the x-z plane. The grid of holes on the table made the fixture mirroring a simple task. The ROMER Arm was used to attain a 4.57 million cloud of points representing the L fender geometry. The point cloud was converted to a mesh suitable for FE analysis through a process summarized in Figure 7-3. The point cloud was exported from Spatial Analyzer in a *.txt* file. MATLAB® was used to mirror the points over the x-z plane. The *.txt* file was imported to PolyWorks where an 8.67 million triangle mesh was generated. The mesh was exported via *.stl* file and imported into the GOM software where many smoothing and patching operations were completed. The final FEA-ready mesh was exported from GOM via *.stl* containing 151,748 nodes and 300,530 triangular shell elements. This mesh was considered S_{des} for the R fender.
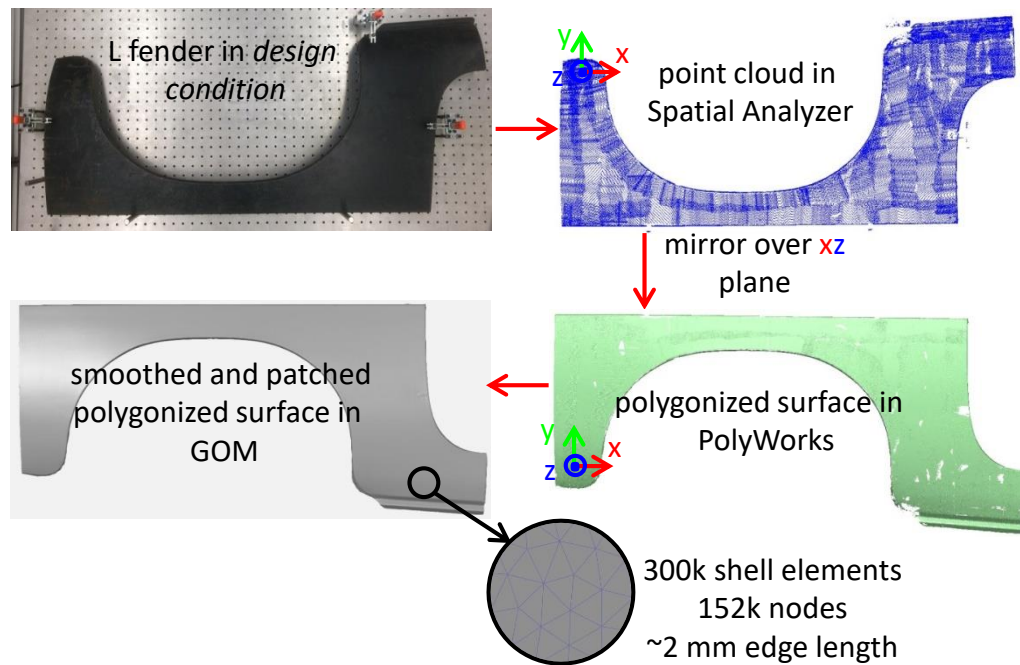
Figure 7-3: Creation of fender CAD geometry, S_{des}

7.2. FEA prediction of D_{meas}, D_{des}, and V

The 300,530 element mesh was imported into Abaqus using the *.stl* import plug-in. The fender was assigned mild steel material properties of Young's modulus 200×10^9 Pa, Poisson's ratio 0.3, and density 7850 kg/m^3. The shell elements were assigned a thickness of 0.95 mm and the default Simpson integration rule with 5 integration points was used. A gravitational load of -9.7976 m/s^2 was created in the z direction. The nodes closest to the fixture locator coordinates were used to define boundary conditions representing each locator (see Figure 7-4). A local coordinate system was created at D1 through D8 in Abaqus such that z represented the surface normal direction. A description of each simulation is provided in Table 7-1 where dn represents movement in the surface normal direction. For all simulations X1 dx = 0, Y1 dy = 0, and Y2 dy = 0.

Applying step 1) from section 6.3 resulted in the gravitational sags shown in Figure 7-5. D_{des} and D_{meas} were represented as dxdydz displacements. The dz components were the largest and are used to visualize the sag in Figure 7-5.

Applying step 2) from section 6.3 the mode shapes that the *design condition* fixture was capable of removing were predicted by FEA. D1, D2, and D3 were considered the *primary* locators while D4 through D8 were considered *supplementary* locators. One mode shape was calculated for the surface normal displacement of each *supplementary* locator (see Table 7-1). The mode shapes are shown in Figure 7-6 where the constrained (dn = 0 mm) locators are red and the displaced (dn = 1 mm) locator is green. The dz component of the dxdydz mode shapes was the largest and is used to visualize the mode shapes in Figure 7-6.

In the fixtureless *measurement condition* (Figure 7-2c), the fender was extremely flexible to rocking motions. Almost zero force was required to cause the fender to rock about the M2 support. A *measurement condition* mode referred to as V_{meas} was used to remove the effects of this rocking motion. V_{meas} was created by constraining M1 through M3 and displacing the corner of the fender 10 mm as described in Table 7-1 and shown in Figure 7-6.

Table 7-1: FE simulation descriptions

Simulation	Load	Boundary conditions
D_{meas}	gravity	M1 through M3 dz = 0
D_{des}	gravity	D1 though D8 dn = 0
V_{meas}	V_{meas} dz = 10 mm	M1 through M3 dz = 0
V_{D4}	D4 dn = 1 mm	D1 though D8 dn = 0, except D4
$\vdots$	$\vdots$	$\vdots$
V_{D8}	D8 dn = 1 mm	D1 though D8 dn = 0, except D8
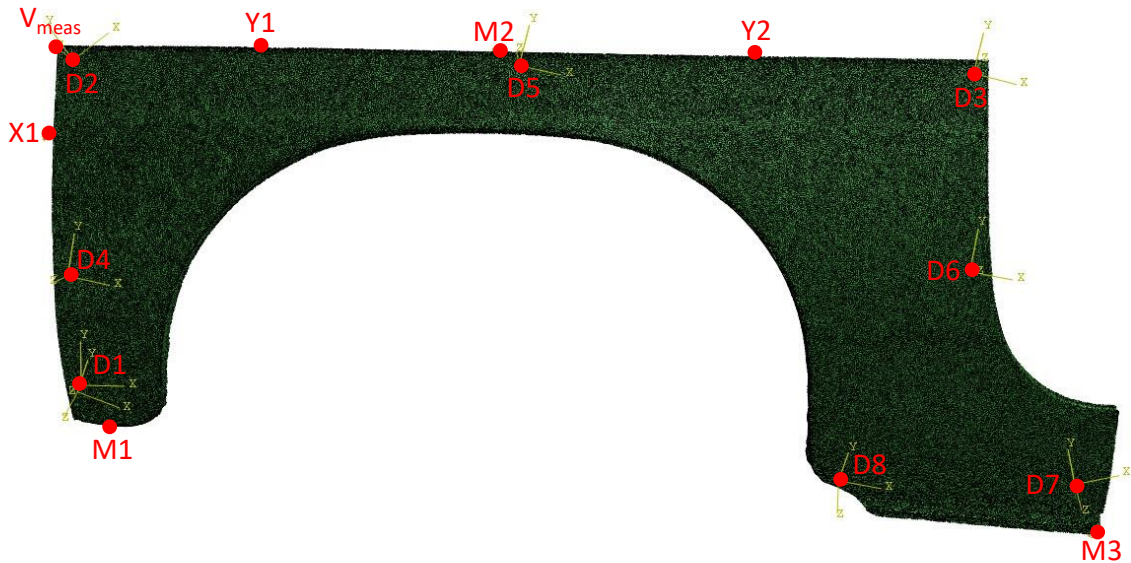
Figure 7-4: FE boundary condition nodes
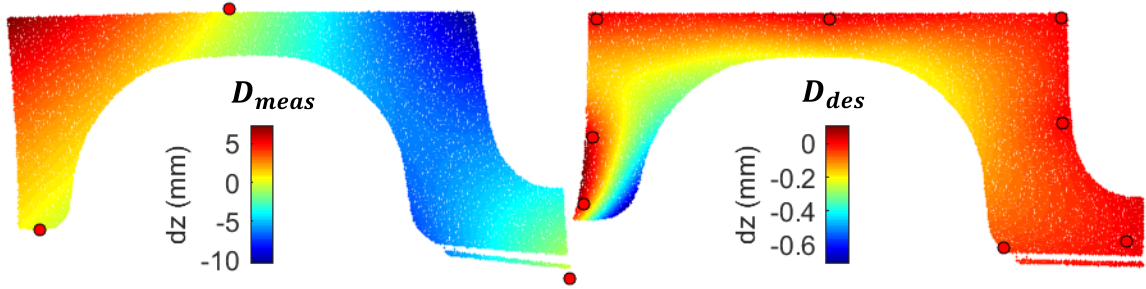
Figure 7-5: Gravitational sag in *measurement* (fixtureless) and *design* (fixtured) conditions, colored by the dz component
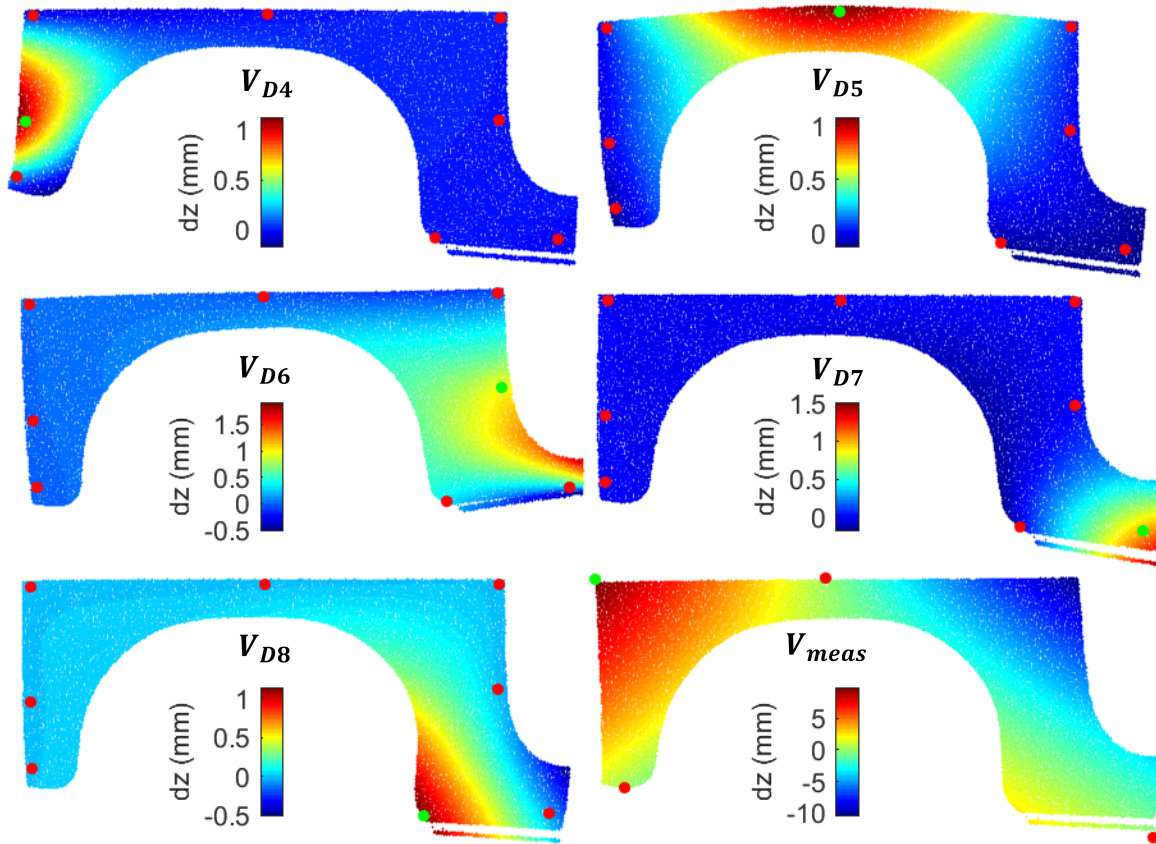
Figure 7-6: Fender mode shapes colored by the dz component

7.3. Mesh preparation for point cloud processing

The region of interest for the profile deviation calculation is the main surface of the fender. The mesh also contains elements representing the ribs on the side of the fender which are not of interest. To improve computational efficiently, the nodes residing on the side ribs were ignored for the profile deviation calculation.

The element size and z component of the nodal normal vector were used to identify the nodes of the mesh corresponding to the side ribs. Element size was smaller in the side rib region and the normal vectors were largely horizontal. By restricting the profile deviation calculation to large elements with a near-vertical normal vector, the side rib regions can be ignored.

Figure 7-7a shows the distribution of element size corresponding to each node. The first peak (side length ≈ 0.5 mm) of the bi-modal distribution represents the fine regions of the mesh around the ribs while the second peak (side length ≈ 2.5 mm) represents the main surface of the mesh. Figure 7-7b shows z component of the nodal normal vector distribution. Setting the element side length threshold to 1.25 mm and normal vector z component threshold to 0.7, the size of the mesh is decreased from 151,748 nodes to 56,748 nodes for profile processing as represented in Figure 7-8. Decreasing the node count to 56,748 reduces the number of loops required in the profile deviation calculation by about 66%.
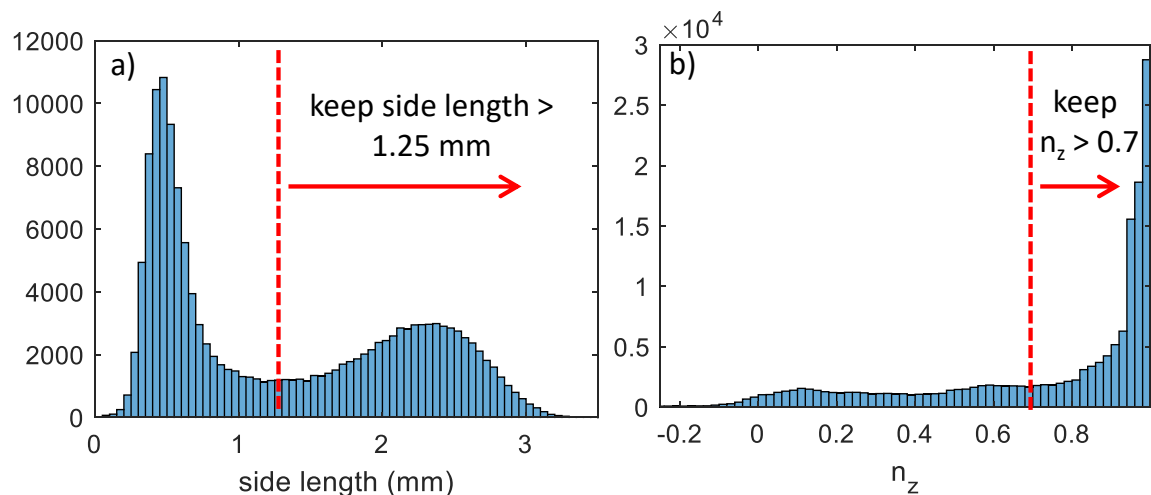
Figure 7-7: Histograms of a) element side length and b) z component of nodal normal vector
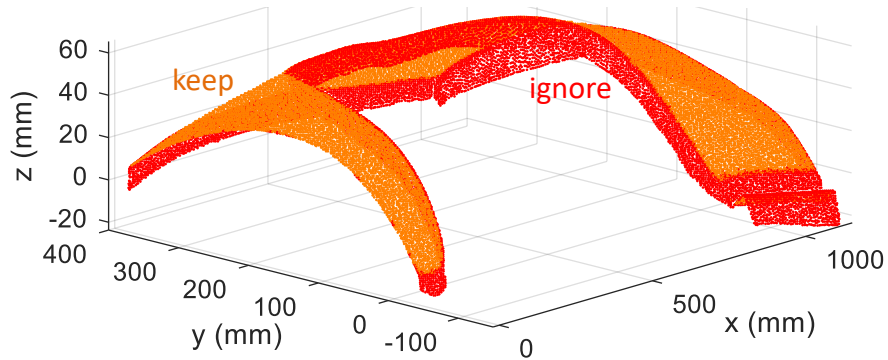
Figure 7-8: Nodes kept for profile deviation processing

7.4. R_{meas} calculation

The point cloud (M_{meas}) for the *measurement condition* profile deviation (R_{meas}, the measurand) was measured with the fender in the fixtureless *measurement condition* (Figure 7-2c) and contained 4.60 million points. Step 3) of section 6.3 was completed by using a z-roll-pitch best-fit transformation of S_{meas} and addition of the V_{meas} mode to minimize the surface normal distances between M_{meas} and S_{meas} at D1, D2, D3, and a location near the bottom right of the fender. The position near the bottom right of the fender was chosen as an arbitrary location for V_{meas} to remove *the measurement condition* "zero force" twist.

This process resulted in the transformed surface $S_{meas,T}$ and is shown in Figure 7-9. Blue vectors in the figure represent the surface normal direction. Overlaying the coordinate systems served to roughly align M_{meas} to S_{meas} resulting in Figure 7-9a. The MATLAB® *fminsearch* function transformed S_{meas} and added C*V_{meas} to minimize the surface normal distance at the four locations in Figure 7-9a. MATLAB® (see code in Appendix C.1) reported the final V_{meas} coefficient as -0.96. Figure 7-9b shows the resulting $S_{meas,T}$ contacting the point cloud at the four normal vectors.
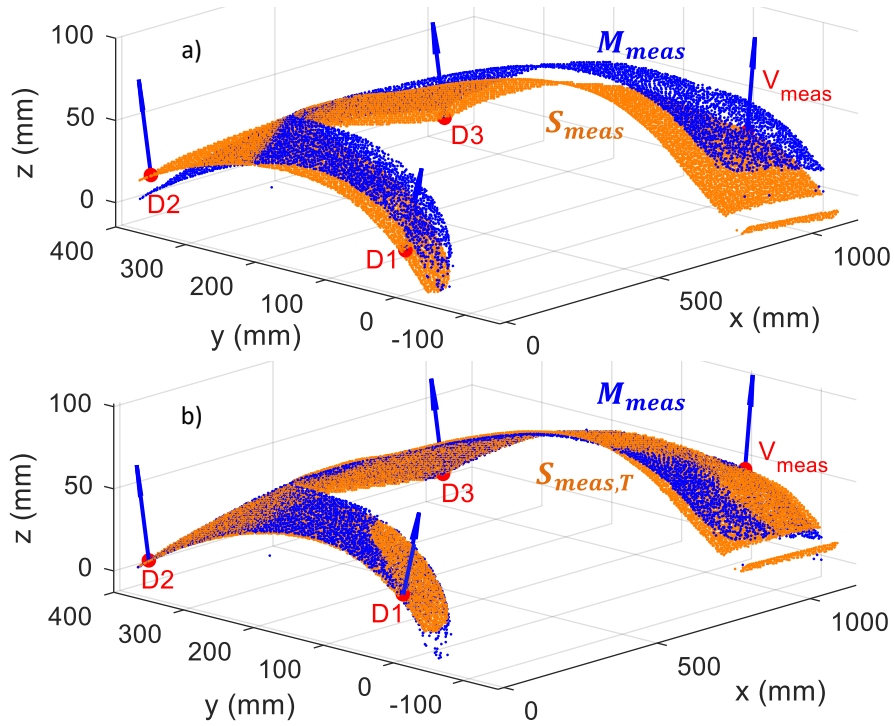
Figure 7-9: Step 3) of section 6.3, alignment of S_{meas} to M_{meas} creating $S_{meas,T}$, a) before and b) after

Applying step 4) of section 6.3, $S_{meas,T}$ (Figure 7-9b) was scaled by the "modes" V_{D4} to V_{D8} to create contact between the point cloud and CAD mesh at the *supplementary* locators D4 through D8. The resultant surface $S_{meas,V}$ is shown in Figure 7-10. The MATLAB® code to accomplish this step is provided in Appendix C.2.
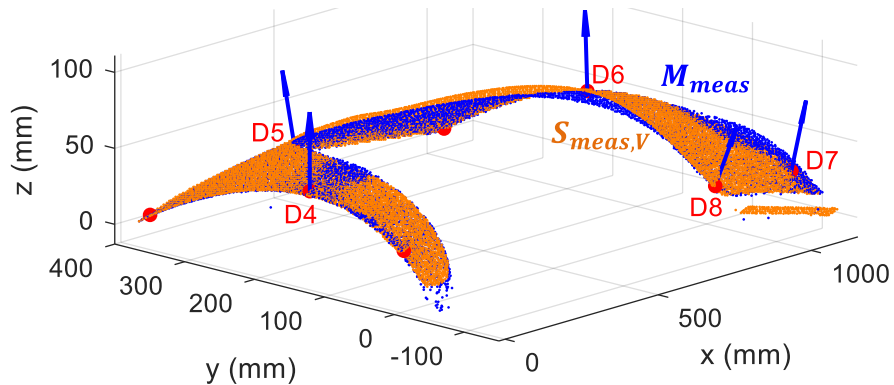
Figure 7-10: Scaling of $S_{meas,T}$ to create contact between $S_{meas,V}$ and M_{meas} at D4 through D8 (step 4) of section 6.3)

71

The mode coefficients required to create contact at D4 through D8 are reported in Table 7-2. Since each mode was created from 1 mm surface normal displacements (Table 7-1), the coefficients are simply the surface normal distance in millimeters between $S_{meas,T}$ and M_{meas}. In Figure 7-9b for example, 8.9 mm of surface normal displacement is required to create contact between $S_{meas,T}$ and M_{meas} at the D8 location. After adding $C_{D8}*V_{D8}$ contact is created at D8 in Figure 7-10.

Table 7-2: Mode coefficients

C_{D4}	1.35
C_{D5}	1.34
C_{D6}	0.43
C_{D7}	-4.43
C_{D8}	8.90

Applying step 5) of section 6.3, the coefficients from Table 7-2 are used to predict the assembly forces. The predicted assembly forces (using the code in Appendix C.2) are reported in Table 7-3. While no experimental forces were measured to compare to the predicted assembly forces, the negative surface normal forces (Fn) at D4, D6, and D8 indicate a clamp is required to push the fender into contact with the locator. This is consistent with the required clamp locations in the fixture (Figure 7-2b) which confirms the sign of the predicted surface normal forces are correct.

Table 7-3: Predicted assembly forces (units: N)

Locator	Fx	Fy	Fz	Fn
D1	-0.44	-2.19	4.54	5.06
D2	-0.56	2.34	8.31	8.65
D3	0.52	4.36	13.57	14.26
D4	0.19	0.07	-2.20	-2.21
D5	0.00	-0.01	-0.04	-0.04
D6	-0.59	-1.51	-16.70	-16.78
D7	0.41	-6.42	15.51	16.79
D8	0.07	0.71	-0.96	-1.20

Finally, applying step 6) of section 6.3, the profile deviation R_{meas} was calculated using the MATLAB® code in Appendix C.3. The cylindrical search radius (R) was set to 1 mm, the standard deviation (σ_i) threshold to 0.05 mm, and the nearest neighbor (Q_i) threshold to 10. The calculations were performed on an Intel® Core i7-3720QM CPU @ 2.60 GHz and took 5,657 seconds of CPU time and 36 minutes of physical time for the 4.60 million point M_{meas} and 56,748 node S_{meas}. The resulting R_{meas} is shown in Figure 7-11.
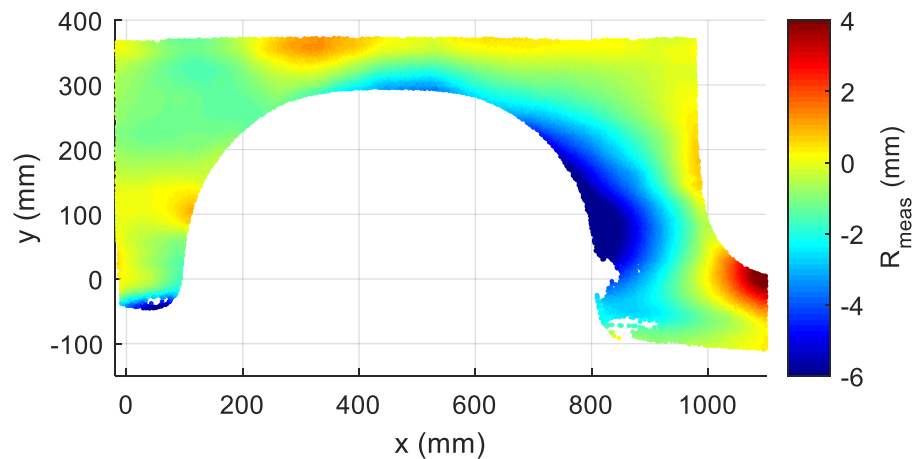
Figure 7-11: Profile deviation measurand R_{meas}

7.5. R_{des} calculation

The point cloud (M_{des}) for the *design condition* profile deviation (R_{des}, check of the measurand) was measured with the fender in the *design condition* fixture (Figure 7-2b) and contained 4.92 million points. The point cloud (M_{des}) was aligned to the *design condition* CAD model (S_{des}) through a z-roll-pitch best-fit transformation that minimized the sum of the squared z distances at D1, D2, D3, D5, and D7 using the MATLAB® *fminsearch* function. D4, D6, and D8 could not be used because the point cloud was insufficiently dense due to obstruction of the scanner view by the clamps (see the clamps in Figure 7-2d).

73

The profile deviation was evaluated using the code in Appendix C.3 with the same settings as the R_{meas} calculation. The calculations took 5,996 seconds of CPU time and 39 minutes of physical time for the 4.92 million point M_{des} and 56,748 node S_{des}. The resulting R_{des} is shown in Figure 7-12.
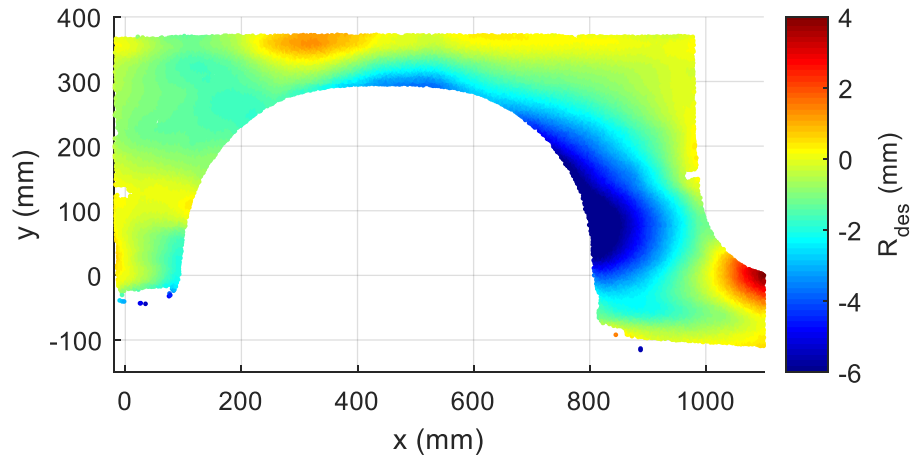
Figure 7-12: Profile deviation check of measurand R_{des}

7.6. Performance evaluation

The measurand (R_{meas}, Figure 7-11) and the check of the measurand (R_{des}, Figure 7-12) are compared in Figure 7-13. The histogram and the statistics in Table 7-4 reveal that 95% of the deltas lie between -0.31 mm and 0.63 mm. Compared to the 6 mm profile deviations (Figure 7-12) and 10 mm *measurement condition* deflections (Figure 7-5), this is considered a success. The proposed approach was able to attain the profile deviation in a fixtureless condition that matched the "true" profile deviation within 0.63 mm, an order of magnitude lower that the background deflections or profile deviation.
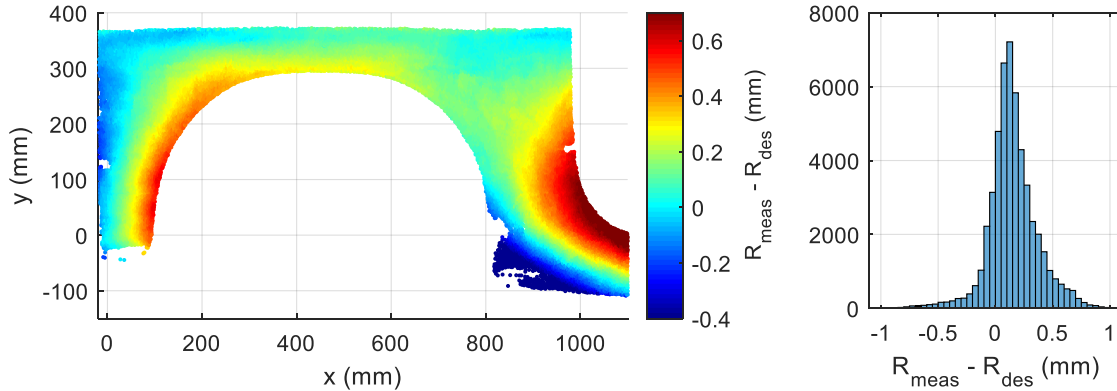
Figure 7-13: Delta between R_{meas} and R_{des}

Table 7-4: Statistics relating to profile deviation calculation results

Variable		Mean	Std. dev.	Min	Percentiles				Max
					2.5%	16%	84%	97.5%	
R_{meas} - R_{des} (mm)		0.15	0.22	-1.20	-0.30	-0.01	0.34	0.63	1.16
Measurement condition	σ_i (mm)	0.029	0.013	0.000	0.012	0.019	0.039	0.058	0.366
	Q_i	55.6	30.2	0	4	31	79	131	367
Design condition	σ_i (mm)	0.026	0.016	0.000	0.010	0.016	0.034	0.057	0.628
	Q_i	59.1	33.0	0	2	31	87	136	420

The standard deviation per node in the *measurement condition* is shown in Figure

7-14 and the statistics are listed in Table 7-4. Regions of high standard deviation occurred

near the bottom of the fender where incidence angle and surface finish provided a

challenging measurement for the ROMER Arm scanner. The number of nearest cloud

point neighbors within the cylindrical search volume in the *measurement condition* is

shown in Figure 7-15 and the statistics are listed in Table 7-4. Manual scanning with the

ROMER Arm created an inhomogeneous distribution of point cloud density. Regions

with standard deviation greater than 0.05 mm or number of points less than 10 were

ignored causing the profile deviation data gaps in Figure 7-11.
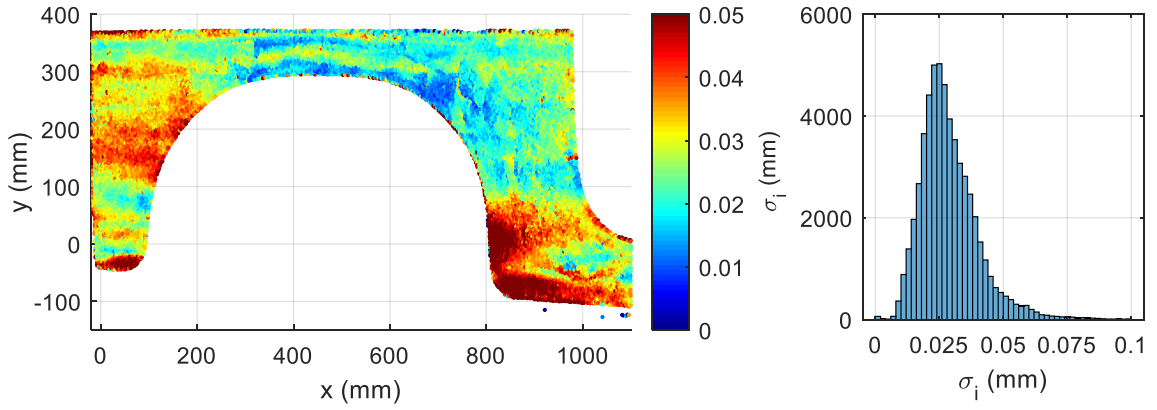
Figure 7-14: Standard deviation per node for the *measurement condition*
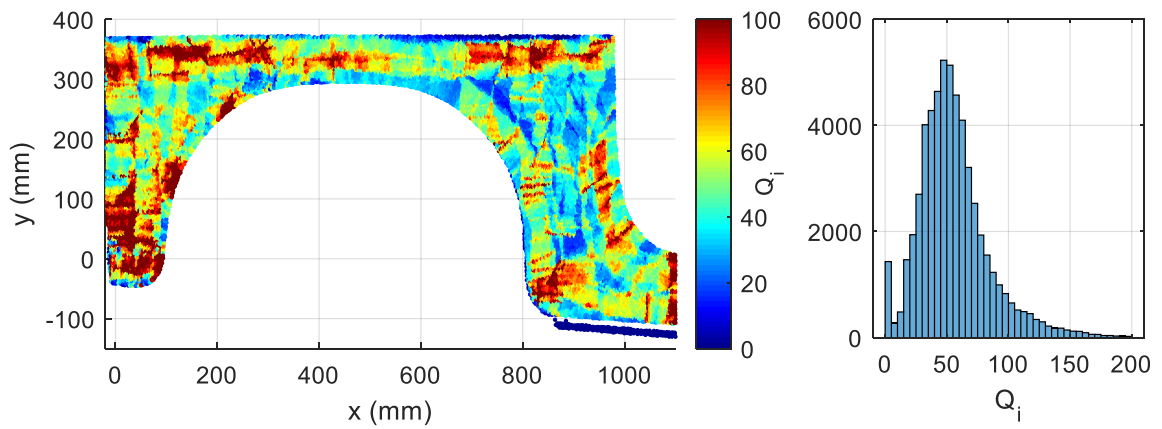
Figure 7-15: The number of nearest cloud point neighbors per node for the *measurement condition*

CHAPTER 8: CONCLUSION AND FUTURE WORK

In 2002 the research area of fixtureless inspection for nonrigid parts emerged in the literature. Over the past fifteen years, over thirty papers have been published in this area with the goal of enabling the dimensional inspection of nonrigid parts without using specialized fixtures. Many methods have been tested including a range of FE and non-FE based approaches. This thesis sought to build on the literature by applying fixtureless inspection to an automotive part, using real measured data (rather than simulated data), completing an uncertainty analysis, and providing a means to calculate the assembly forces. This thesis also thoroughly documents all of the equations and processing codes used which could be adopted by future researchers.

The point cloud processing method from Thiébaut et al. [34] was applied to a cantilevered flat plate. The profile deviation from the nonrigid inspection method agreed with the directly measured profile deviation to within 25 μm (Figure 4-9, Table 4-2). An uncertainty analysis showed that the uncertainty in the profile deviation reaches a maximum of 48 μm at the free end of the plate with the uncertainty in the thickness and modulus of elasticity being the largest contributors (Table 5-2).

A new approach for correcting the fixtureless inspection method for mode shapes removed by the *design condition* fixture was developed by conceptually investigating the measurement of a saddle-shaped plate. This new approach was applied to the inspection of an automotive fender. The profile deviation from the fixtureless inspection method agreed with the directly measured profile deviation to between -0.31 mm and 0.63 mm (Figure 7-13, Table 7-4). This is a promising first result considering the *measurement*

condition fender sag reaches 10 mm (Figure 7-5) and the directly measured profile

deviation reaches 6 mm (Figure 7-12).

This method also has the potential to be computationally efficient. From section

6.3, this method is unique from many others in the literature in that the pre-processing

FEA steps only need to be completed once per part design. The FEA simulations take

about 5 minutes each for the fender mesh so avoiding the need to complete FEA for every

part is important for real-time inspection. The remaining processing steps need to be

completed for every measured part. The computational time to process the fender data

which contained over 50,000 nodes and over 4 million points took almost 40 minutes (see

section 7.4). Metrologists from industry should be consulted to select a subset of the

50,000 nodes that are important for the profile deviation measurement. For example, if

the profile deviation measurement was limited to 100 nodes, the point cloud processing

computational time should decrease to about 5 seconds which is acceptable for real-time

inspection in a production environment.

8.1. Future work

Several activities should be completed to thoroughly evaluate the proposed

fixtureless inspection approach. An instrumented fixture that measures the assembly

forces at each fixture locator should be constructed to increase the confidence in the

assembly force calculations. This activity would likely lead to a better understanding of

assembly forces allowing the proposed approach to be adjusted for more accurate force

prediction. The accuracy of the predicted mode shapes should also be quantified by

modifying the fixture to bend the fender into one of the mode shapes and then measuring

and comparing to the FE predicted mode shapes. An uncertainty analysis of the fender

should be completed to identify the primary factors that need to be addressed for improved accuracy. The approach should be applied to on an automotive part with a real CAD model and a real inspection fixture currently used in a production environment.

To increase the industrial applicability, the accuracy needs to be improved such that the profile deviation from the nonrigid inspection method agrees with the directly measured profile deviation to within 0.1 mm. The scanning process should also be automated using a faster scanner type such as a fringe projection system. The computational efficiency of the initial CAD model to point cloud registration code (section 7.4, Appendix C.1) should also be improved. It currently takes over 30 seconds to execute because the MATLAB® *fminsearch* optimization code is used for alignment. A deterministic code for this alignment should be written which would likely decrease the computational time for the CAD to point cloud alignment to less than 1 second. If the point cloud processing step (section 7.4, Appendix C.3) was limited to 100 nodes such that the computational time decreased to 5 seconds, the entire process could be completed in less than 7 seconds (on a ThinkPad T530 laptop with i7-3720QM CPU).

There are many applications yet to be explored in the literature that could benefit from fixtureless inspection or, more generally, the FE correction of dimensional metrology data. For example, the prediction of the shape of space-based structures when measured under the influence of gravity on earth, as briefly mentioned in ref: [6]. Also, nonrigid parts of much larger scale can benefit from the ability to correct dimensional metrology data for gravitational sag (for example ref: [42]). Any part where the design loads, constraints, or gravity cause part deformations greater than 1/10 of the dimensional tolerance can be benefit from this process.

REFERENCES

[1]   American Society of Mechanical Engineers, "ASME Y14.5-2009: Dimensioning and Tolerancing," 2009.

[2]   G. N. Abenhaim, A. Desrochers, and A. Tahan, "Nonrigid parts' specification and inspection methods: Notions, challenges, and recent advancements," *Int. J. Adv. Manuf. Technol.*, vol. 63, no. 5–8, pp. 741–752, 2012.

[3]   A. Jaramillo, P. Boulanger, and F. Prieto, "On-line 3-D system for the inspection of deformable parts," *Int. J. Adv. Manuf. Technol.*, vol. 57, no. 9–12, pp. 1053–1063, 2011.

[4]   R. Ascione and W. Polini, "Measurement of nonrigid freeform surfaces by coordinate measuring machine," *Int. J. Adv. Manuf. Technol.*, vol. 51, no. 9–12, pp. 1055–1067, 2010.

[5]   V. Sabri, S. A. Tahan, X. T. Pham, D. Moreau, and S. Galibois, "Fixtureless profile inspection of non-rigid parts using the numerical inspection fixture with improved definition of displacement boundary conditions," *Int. J. Adv. Manuf. Technol.*, vol. 82, no. 5–8, pp. 1343–1352, 2016.

[6]   K. Blaedel, D. Swift, A. Claudet, E. Kasper, and S. Petterson, "Metrology of Non-Rigid Objects," 2002.

[7]   A. Weckenmann and A. Gabbia, "Testing formed sheet metal parts using fringe projection and evaluation by virtual distortion compensation," in *Fringe 2005*, 2006, pp. 539–546.

[8]   A. Weckenmann, P. Gall, and A. Gabbia, "3D surface coordinate inspection of formed sheet material parts using optical measurement systems and virtual distortion compensation," in *Eighth International Conference on Laser Metrology*, 2005, p. 640.

[9]   A. Weckenmann, J. Weickmann, and N. Petrovic, "Shortening of Inspection Processes by Virtual Reverse Deformation," in *4Th International Conference and Exhibition on Design and Production of Machines and Dies/Molds*, 2007, pp. 21–23.

[10]   A. Jaramillo, P. Boulanger, and F. Prieto, "On-line 3-D inspection of deformable parts using FEM trained radial basis functions," in *2009 IEEE 12th International Conference on Computer Vision Workshops, ICCV Workshops 2009*, 2009, pp. 1733–1739.

[11]   A. Jaramillo, F. Prieto, and P. Boulanger, "Fast dimensional inspection of deformable parts from partial views," *Comput. Ind.*, vol. 64, no. 9, pp. 1076–1081, 2013.

[12] A. Jaramillo, F. Prieto, and P. Boulanger, "Fixtureless inspection of deformable parts using partial captures," *Int. J. Precis. Eng. Manuf.*, vol. 14, no. 1, pp. 77–83, 2013.

[13] S. Lemeš, "Validation of numerical simulations by digital scanning of 3D sheet metal objects," University Of Ljubljana, 2010.

[14] I. E. C. BIPM, I. IFCC, I. IUPAC, and O. ISO, "Evaluation of measurement data - guide for the expression of uncertainty in measurement," *JCGM 1002008*, 2008.

[15] I. Gentilini and K. Shimada, "Predicting and evaluating the post-assembly shape of thin-walled components via 3D laser digitization and FEA simulation of the assembly process," *CAD Comput. Aided Des.*, vol. 43, no. 3, pp. 316–328, 2011.

[16] G. N. Abenhaim, A. Tahan, A. Desrochers, and R. Maranzana, "A Novel Approach for the Inspection of Flexible Parts Without the Use of Special Fixtures," *J. Manuf. Sci. Eng.*, vol. 133, no. 1, p. 011009, 2011.

[17] A. Aidibe, A. Tahan, and G. N. Abenhaim, "Dimensioning control of non-rigid parts using the Iterative Displacement Inspection with the maximum normed residual test," *WSEAS Trans. Appl. Theor. Mech.*, no. Recent Researches in Mechanics, 2011.

[18] H. Radvar-Esfahlan and S. A. Tahan, "Nonrigid geometric metrology using generalized numerical inspection fixtures," *Precis. Eng.*, vol. 36, no. 1, pp. 1–9, 2012.

[19] H. Radvar-Esfahlan and S. A. Tahan, "Robust generalized numerical inspection fixture for the metrology of compliant mechanical parts," *Int. J. Adv. Manuf. Technol.*, vol. 70, no. 5–8, pp. 1101–1112, 2014.

[20] H. Radvar-Esfahlan and S. -a. Tahan, "Performance study of dimensionality reduction methods for metrology of nonrigid mechanical parts," *Int. J. Metrol. Qual. Eng.*, vol. 4, no. 3, pp. 193–200, 2014.

[21] H. Radvar-Esfahlan, "Fixtureless geometric inspection of nonrigid parts using 'generalized numerical inspection fixture,'" École De Technologie Supérieure Université Du Québec, 2014.

[22] G. N. Abenhaim, S. A. Tahan, A. Desrochers, and J.-F. Lalonde, "Aerospace Panels Fixtureless Inspection Methods with Restraining Force Requirements; A Technology Review," *SAE Tech. Pap.*, 2013.

[23] A. Aidibe and A. Tahan, "The inspection of deformable bodies using curvature estimation and Thompson-Biweight test," *Int. J. Adv. Manuf. Technol.*, vol. 71, no. 9–12, pp. 1733–1747, 2014.

[24] A. Aidibe and A. Tahan, "Adapting the coherent point drift algorithm to the fixtureless dimensional inspection of compliant parts," *Int. J. Adv. Manuf. Technol.*, vol. 79, no. 5–8, pp. 831–841, 2015.

[25] K. Babanezhad, G. Foucault, A. Tahan, and J. Bigeon, "A Bi-criterion Flexible Registration Method for Fixtureless Inspection of Compliant Parts," *Procedia CIRP*, vol. 46, pp. 307–310, 2016.

[26] G. N. Abenhaim, A. Desrochers, A. S. Tahan, and J. Bigeon, "A virtual fixture using a FE-based transformation model embedded into a constrained optimization for the dimensional inspection of nonrigid parts," *CAD Comput. Aided Des.*, vol. 62, pp. 248–258, 2015.

[27] G. N. Abenhaim, A. Desrochers, A. S. Tahan, and J. Bigeon, "A Finite-Element Boundary Condition Setting Method for the Virtual Mounting of Compliant Components," *J. Comput. Inf. Sci. Eng.*, vol. 15, no. 4, p. 041005, 2015.

[28] S. S. Karganroudi, J. C. Cuillière, V. Francois, and S. A. Tahan, "Automatic fixtureless inspection of non-rigid parts based on filtering registration points," *Int. J. Adv. Manuf. Technol.*, vol. 87, pp. 687–712, 2016.

[29] S. S. Karganroudi, J.-C. Cuillière, V. François, and S.-A. Tahan, "Assessment of the Robustness of a Fixtureless Inspection Method for Nonrigid Parts Based on a Verification and Validation Approach," *J. Verif. Valid. Uncertain. Quantif.*, vol. 2, no. 4, p. 041002, 2018.

[30] S. S. Karganroudi, J. C. Cuillière, V. François, and S. A. Tahan, "'What-if' scenarios towards virtual assembly-state mounting for non-rigid parts inspection using permissible loads," *Int. J. Adv. Manuf. Technol.*, vol. 97, no. 1–4, pp. 353–373, 2018.

[31] V. Sabri, "Dimensional Metrology of Non-rigid Parts without Specialized Inspection Fixtures," École De Technologie Supérieure Université Du Québec, 2017.

[32] V. Sabri, S. A. Tahan, X. T. Pham, H. Radvar-Esfahlan, B. Louhichi, and A. M. Tahvilian, "Fixtureless profile inspection of non-rigid parts," in *CIE43 Proceedings*, 2013, no. October, p. 71.

[33] V. Sabri, S. Sattarpanah, S. A. Tahan, J. C. Cuillière, V. François, and X. T. Pham, "A robust and automated FE-based method for fixtureless dimensional metrology of non-rigid parts using an improved numerical inspection fixture," *Int. J. Adv. Manuf. Technol.*, vol. 92, no. 5–8, pp. 2411–2423, 2017.

[34] F. Thiébaut, C. Lacroix, L. Andolfatto, and C. Lartigue, "Evaluation of the shape deviation of non rigid parts from optical measurements," *Int. J. Adv. Manuf. Technol.*, vol. 88, no. 5–8, pp. 1937–1944, 2017.

[35] C. Lartigue, F. Thiébaut, P. Bourdet, and N. Anwer, "Dimensional metrology of flexible parts: identification of geometrical deviations from optical measurements," *Adv. Math. Comput. tools Metrol. VII*, pp. 196–203, 2006.

[36] E. Savio, L. De Chiffre, and R. Schmitt, "Metrology of freeform shaped parts," *CIRP Ann. - Manuf. Technol.*, vol. 56, no. 2, pp. 810–835, 2007.

[37] Y. Li and P. Gu, "Free-form surface inspection techniques state of the art review," *CAD Comput. Aided Des.*, vol. 36, no. 13, pp. 1395–1417, 2004.

[38] F. Beer, R. Johnston, J. DeWolf, and D. Mazurek, *Mechanics of Materials*, Sixth. New York, NY: McGraw-Hill, 2012.

[39] National Imagery and Mapping Agency, "Department of Defense World Geodetic System 1984, Third Edition."

[40] Wikipedia, "Bouguer anomaly." [Online]. Available: https://en.wikipedia.org/wiki/Bouguer_anomaly. [Accessed: 20-Oct-2018].

[41] Wikipedia, "Gravity anomaly." [Online]. Available: https://en.wikipedia.org/wiki/Gravity_anomaly. [Accessed: 20-Oct-2018].

[42] M. Erickson, "Demonstration of a closed loop digitally enabled manufacturing process using advanced metrology techniques," University of North Carolina at Charlotte, 2018.

[43] T. Jirka and V. Skala, "Gradient vector estimation and vertex normal computation," *Szczyrk Int. Work.*, pp. 27–32, 2003.

APPENDIX A: PROFILE DEVIATION CALCULATION DETAILS

A.1. Normal vector computation

The unit normal vector computation for a given node, mentioned in section 2.2 step 2), was completed using one of the techniques documented by Jirka and Skala [43]. This method simply averages the normal vectors of the elements in which the node is a part of to estimate the normal vector for that node. This process is described in Figure A-1.

$$\vec{n} = \frac{\sum_{g=1}^{h} \vec{A}_g}{\left| \sum_{g=1}^{h} \vec{A}_g \right|}$$

$\vec{A}_h$: surface normal of element p
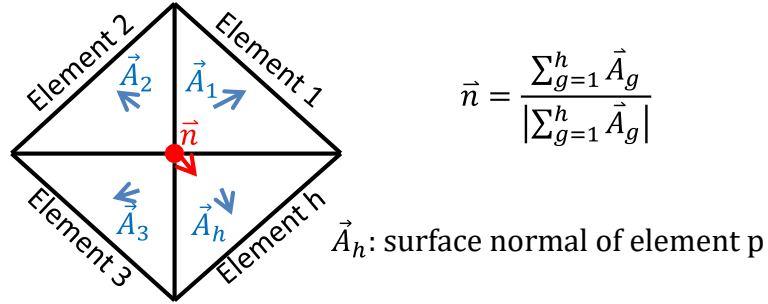
Figure A-1: Nodal normal vector computation

A.2. Point cloud nearest neighbor search

The search for the nearest neighbors, mentioned in section 2.2 step 3), is illustrated in Figure A-2. Let $\overrightarrow{M_{meas\,j}}$ be the vector between the ith node of $\boldsymbol{S_{meas}}$ to the jth point of the point cloud $\boldsymbol{M_{meas}}$ (recall Figure 2-3). The distance D between $M_{meas\,j}$ and $\vec{n}_i$ can then be calculated according to Figure A-2. Now, only $\boldsymbol{M_{meas}}$ cloud points within the cylindrical radius R (i.e. $D < R$) are stored in $\boldsymbol{N}$ (recall Figure 2-3c) which is a $q x 3$ matrix containing the XYZ coordinates of the nearest cloud point neighbors. The index into $\boldsymbol{N}$ is k.

$$D = \sqrt{\left|\overrightarrow{M_{meas_j}}\right|^2 - \left(\overrightarrow{M_{meas_j}} \cdot \vec{n_i}\right)^2}$$
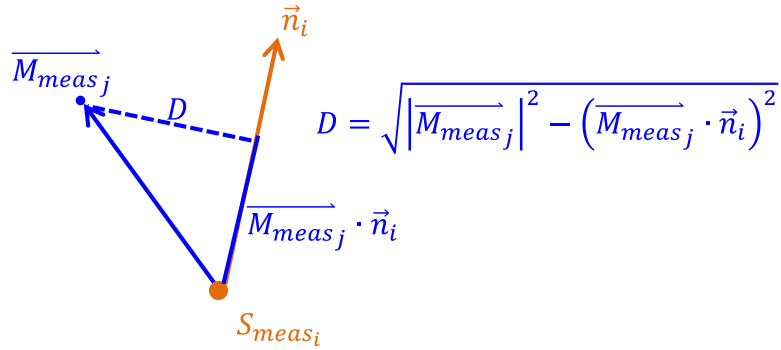
Figure A-2: Calculation of nearest neighbor distance

A.3. MATLAB code for profile deviation calculation

The MATLAB code for the profile deviation calculation shown below

accomplishes step 3) through step 8) of section 2.2.

```
function [results] = process(Smeas,Mmeas,n,R,sigt,Qt)
%n - unit surface normal vector for each node of Smeas
%R - cylindrical search radius
%sigt - standard deviation threshold
%Qt - number of nearest neighbors threshold

%preallocate array sizes for computational efficiency
Rmeas = zeros(length(Smeas.Node),1);
sig = zeros(length(Smeas.Node),1);
Q = zeros(length(Smeas.Node),1);

for i = 1:length(Smeas.Node)%check each node
    %step 3: find nearest point cloud neighbors
    Mmeasj = [(Mmeas(:,1)-Smeas.X(i)) (Mmeas(:,2)-Smeas.Y(i))
        (Mmeas(:,3)-Smeas.Z(i))];
    Mmeasj_n = Mmeasj(:,1).*n(i,1)+Mmeasj(:,2).*n(i,2)+
        Mmeasj(:,3).*n(i,3);%Mmeasj dot product with n
    Mmeasj_mag = sqrt(sum(Mmeasj.^2,2));
    D = sqrt(Mmeasj_mag.^2 - Mmeasj_n.^2);
    TF = D<R;%find points within cylindrical radius

    %step 4: fetch surface normal distance for each nearest neighbor
    e = Mmeasj_n(TF);%keeps only the true elements

    %step 5: calculate profile deviation
    Rmeas(i,1) = mean(e);

    %step 6: calculate standard deviation
    sig(i,1) = std(e);

    %step 7: store number of nearest neighbors
    Q(i,1) = length(e);
    i%output node number for status update
```

```matlab
    end

    %step 8: check Qt and sigt thresholds
    fail = Q<Qt | sig>sigt;
    Rmeas(fail) = NaN;%ignore deviations which don't meet thresholds

    vars = {'Rmeas','sig','Q'};
    results = table(Rmeas,sig,Q);
    results.Properties.VariableNames = vars;
end
```

APPENDIX B: CANTILEVERED FLAT PLATE MATLAB CODE

B.1. MATLAB code for point cloud simplification

The following MATLAB code finds the cloud points from M_{meas} within a 1mm XY radius of the S_{meas} mesh nodes. The identified cloud points are then averaged to return a single cloud point for that node. The resulting simplified point cloud called $M_{meas,node}$ is an $mx3$ matrix containing the XYZ coordinates. An equivalent code was used to convert M_{des} and S_{des} into $M_{des,node}$. Refer to section 4.3 to see how this fits into the narrative.

```matlab
load('Smeas.mat')
load('Mmeas.mat')
[Mmeas_node] = process(Smeas,Mmeas,1);

function [cloud_node] = process(mesh,cloud,R)
for i = 1:length(mesh.Node)%check each Pi (node)
    X = mesh.X(i); Y = mesh.Y(i);
    r = sqrt((cloud.X-X).^2 + (cloud.Y-Y).^2);
    TF = r<R;%calculate a logical array for cylinder radius

    x = mean(cloud.X(TF));
    y = mean(cloud.Y(TF));
    z = mean(cloud.Z(TF));

    cloud_node(i,:) = [x y z];
end
end
```

B.2. MATLAB code for point cloud registration

The following MATLAB code was used for the transformation of the simplified M_{meas} (output from the Appendix B.1 code) to S_{meas} by using the MATLAB *fminsearch* function to minimize the sum of the squared Z deltas. Rotations about X and Y and translations in Z were used. The code output *trans* which contained the resulting best fit XY rotations and Z translation. An equivalent code was used to transform the simplified M_{des} to S_{des}. Refer to section 4.3 to see how this fits into the narrative.

87

```matlab
trans0 = [0 0 0];%all initial guesses = 0
options = optimset('TolFun',1e-7,'MaxFunEvals',1e4,'TolX',1e-7);
[trans,fval,exitflag,output] = fminsearch(@transform,trans0,options)

function [sum_squares] = transform(trans)
%O denotes original coordinate system
%T denotes transformed coordinate system
load('Smeas.mat')
load('Mmeas_node.mat')

z = trans(1);
alpha = trans(2);
beta = trans(3);

R_OTy = [cos(beta) 0 -sin(beta); 0 1 0; sin(beta) 0 cos(beta)];
R_OTx = [1 0 0; 0 cos(alpha) sin(alpha); 0 -sin(alpha) cos(alpha)];
O_T = [0 0 z]';

Mmeas_node_T = O_T + R_OTx*R_OTy*Mmeas_node';
Mmeas_node_T = Mmeas_node_T';

squares = (Mmeas_node_T(:,3)-Smeas.Z).^2;
sum_squares = sum(squares,'omitnan');
end
```

APPENDIX C: FENDER MATLAB CODE

C.1. MATLAB code for $S_{meas,T}$

The following MATLAB code transforms S_{meas} to contact M_{meas} at D1 to D3 and adds C*V_{meas} to create contact at an arbitrary node near the bottom right of the fender (see Figure 7-9b). $S_{meas,T}$ is output. The initial guess listed in the code below is the final result output from the code after many iterations. This code accomplishes step 3) of section 6.3. Refer to section 7.4 to see how this fits into the narrative.

```
load('Smeas.mat')
load('n.mat')
Mmeas = readtable('Mmeas.txt');


trans0 = [16.0799    0.0489   -0.0007   -0.9596];%initial guesses
options = optimset('TolFun',1e-7,'MaxFunEvals',1e4,'TolX',1e-7);
trans = transform1(trans0,options,Smeas,n,Mmeas)

function trans = transform1(trans0,options,Smeas,n,Mmeas)
nodes = [808 24607 140118 146186]%node numbers for D1,D2,D3, and Vmeas
R=1;%search radius (mm)
[trans,fval,exitflag,output] = fminsearch(@transform,trans0,options)

function [sum_surf_norms] = transform(trans)
%O denotes original coordinate system
%T denotes transformed coordinate system

%fetch transformation values
z = trans(1);%z translation (mm)
alpha = trans(2);%x rotation (rad)
beta = trans(3);%y rotation (rad)
C = trans(4);%Vmeas coefficient (unitless)

R_OTy = [cos(beta) 0 -sin(beta); 0 1 0; sin(beta) 0 cos(beta)];
R_OTx = [1 0 0; 0 cos(alpha) sin(alpha); 0 -sin(alpha) cos(alpha)];
O_T = [0 0 z]';%vector from T origin to O origin

Smeas_T(:,1) = Smeas.x + C*V.meas.dx;
Smeas_T(:,2) = Smeas.y + C*V.meas.dy;
Smeas_T(:,3) = Smeas.z + C*V.meas.dz;
Smeas_T = O_T + R_OTx*R_OTy*Smeas_T';
Smeas_T = Smeas_T';

for i = 1:4%complete loop for D1,D2,D3,and Vmeas
    dx = Mmeas.x-Smeas_T(nodes(i),1);
    dy = Mmeas.y-Smeas_T(nodes(i),2);
    XY = abs(dx)<10 & abs(dy)<10;%find cloud points within 10 mm in xy
```

```
    Mmeasj = [(Mmeas.x(XY)-Smeas_T(nodes(i),1)) (Mmeas.y(XY)-
            Smeas_T(nodes(i),2)) (Mmeas.z(XY)-Smeas_T(nodes(i),3))];
    Mmeasj_n = Mmeasj(:,1).*n(nodes(i),1)+Mmeasj(:,2).*n(nodes(i),2)
            +Mmeasj(:,3).*n(nodes(i),3);%Mmeasj dot product with n
    Mmeasj_mag = sqrt(sum(Mmeasj.^2,2));
    D = sqrt(Mmeasj_mag.^2 - Mmeasj_n.^2);
    TF = D<R;%find points within cylindrical radius

    e = Mmeasj_n(TF);%keeps only the true elements
    surf_norm(i,1) = mean(e);%surface normal distance
end
sum_surf_norms = sum(abs(surf_norm))


end
end
```

C.2. MATLAB code for $S_{meas,V}$

The following MATLAB code scales $S_{meas,T}$ by the mode shapes to contact

M_{meas} at D4 to D8. The assembly forces are also calculated. $S_{meas,V}$ and F are output.

This code accomplishes step 4) and 5) of section 6.3. Refer to section 7.4 to see how this

fits into the narrative.

```
load('Smeas_T.mat')
load('n.mat')
Mmeas = readtable('Mmeas.txt');
load('V')
nodes = [808 24607 140118 10805 60127 129011 124310 73325]%node numbers
    for D1 to D8

R=2;%search radius, when R = 1 mm, C_D8 is NaN, C4 to C7 change by less
    than 1% when R is increased from 1 mm to 2 mm
for i = 4:8%complete loop for D4 to D8
    dx = Mmeas.x-Smeas_T.x(nodes(i));
    dy = Mmeas.y-Smeas_T.y(nodes(i));
    XY = abs(dx)<10 & abs(dy)<10;%find points within +-10 mm in xy

    Mmeasj = [(Mmeas.x(XY)-Smeas_T.x(nodes(i))) (Mmeas.y(XY)-
            Smeas_T.y(nodes(i))) (Mmeas.z(XY)-Smeas_T.z(nodes(i)))];
    Mmeasj_n = Mmeasj(:,1).*n(nodes(i),1)+Mmeasj(:,2).*n(nodes(i),2)
            +Mmeasj(:,3).*n(nodes(i),3);%Mmeasj dot product with n
    Mmeasj_mag = sqrt(sum(Mmeasj.^2,2));
    D = sqrt(Mmeasj_mag.^2 - Mmeasj_n.^2);
    TF = D<R;%find points within cylindrical radius

    e = Mmeasj_n(TF);%keeps only the true elements
    surf_norm(i,1) = mean(e);%surface normal distance
    C(i,1) = surf_norm(i,1);%coefficients for scaling Smeas_T
end
```

```
save('C','C')

Smeas_V = table;
Smeas_V.x = Smeas_T.x + C(4)*V.D4.dx + C(5)*V.D5.dx + C(6)*V.D6.dx +
    C(7)*V.D7.dx + C(8)*V.D8.dx;
Smeas_V.y = Smeas_T.y + C(4)*V.D4.dy + C(5)*V.D5.dy + C(6)*V.D6.dy +
    C(7)*V.D7.dy + C(8)*V.D8.dy;
Smeas_V.z = Smeas_T.z + C(4)*V.D4.dz + C(5)*V.D5.dz + C(6)*V.D6.dz +
    C(7)*V.D7.dz + C(8)*V.D8.dz;
save('Smeas_V','Smeas_V')

load('F')
F_asm = table;
F_asm.Fx = F.Sdes.Fx - C(4)*F.VD4.Fx - C(5)*F.VD5.Fx - C(6)*F.VD6.Fx -
    C(7)*F.VD7.Fx - C(8)*F.VD8.Fx;
F_asm.Fy = F.Sdes.Fy - C(4)*F.VD4.Fy - C(5)*F.VD5.Fy - C(6)*F.VD6.Fy -
    C(7)*F.VD7.Fy - C(8)*F.VD8.Fy;
F_asm.Fz = F.Sdes.Fz - C(4)*F.VD4.Fz - C(5)*F.VD5.Fz - C(6)*F.VD6.Fz -
    C(7)*F.VD7.Fz - C(8)*F.VD8.Fz;
F_asm.Fn = n(nodes,1).*F_asm.Fx + n(nodes,2).*F_asm.Fy +
    n(nodes,3).*F_asm.Fz;
save('F_asm','F_asm')
```

C.3. MATLAB code for R_{meas}

The following MATLAB code calculates the profile deviation by processing

$S_{meas,V}$ against M_{meas}, accomplishing step 6) of section 6.3. Refer to section 7.4 to see

how this fits into the narrative.

```
load('n.mat')
Mmeas = readtable('Mmeas.txt');
load('Smeas_V.mat')

R = 1;%cylindrical radius for search, units: mm
sigt = 0.05;%upper limit on acceptable standard deviation, units: mm
Qt = 10;%lower limit on acceptable nearest neighbor point count

[meas] = process(Smeas_V,Mmeas,n,R,sigt,Qt);
save('meas','meas');%save processed data

function [results] = process(Smeas_V,Mmeas,n,R,sigt,Qt)
%n - unit surface normal vector for each node of Smeas_V
%R - cylindrical search radius
%sigt - standard deviation threshold
%Qt - number of nearest neighbors threshold

%preallocate array sizes for computational efficiency
Rmeas = zeros(length(Smeas_V.x),1);
sig = zeros(length(Smeas_V.x),1);
Q = zeros(length(Smeas_V.x),1);

for i = 1:length(Smeas_V.x)%check each node
```

```matlab
    %steps are numbered to match thesis section 2.2
    %step 3: find nearest point cloud neighbors
    dx = Mmeas.x-Smeas_V.x(i);
    dy = Mmeas.y-Smeas_V.y(i);
    XY = abs(dx)<10 & abs(dy)<10;%find points within 10 mm in xy plane

    Mmeasj = [(Mmeas.x(XY)-Smeas_V.x(i)) (Mmeas.y(XY)-Smeas_V.y(i))
            (Mmeas.z(XY)-Smeas_V.z(i))];
    Mmeasj_n = Mmeasj(:,1).*n(i,1)+Mmeasj(:,2).*n(i,2)+Mmeasj(:,3).*
            n(i,3);%Mmeasj dot product with n
    Mmeasj_mag = sqrt(sum(Mmeasj.^2,2));
    D = sqrt(Mmeasj_mag.^2 - Mmeasj_n.^2);
    TF = D<R;%find points within cylindrical radius

    %step 4: fetch surface normal distance for each nearest neighbor
    e = Mmeasj_n(TF);%keeps only the true elements

    %step 5: calculate profile deviation
    Rmeas(i,1) = mean(e);

    %step 6: calculate standard deviation
    sig(i,1) = std(e);

    %step 7: store number of nearest neighbors
    Q(i,1) = length(e);
    i%output node number for status update
end

%step 8: check Qt and sigt thresholds
fail = Q<Qt | sig>sigt;
Rmeas_unfiltered = Rmeas;
Rmeas(fail) = NaN;%ignore deviations which don't meet thresholds

vars = {'Rmeas_unfiltered','Rmeas','sig','Q'};
results = table(Rmeas_unfiltered,Rmeas,sig,Q);
results.Properties.VariableNames = vars;
end
```